THE EFFECT OF ROCK BRIDGES ON BLASTING FRAGMENTATION IN SEDIMENTARY ROCK

by

Anthony Michael LeBaron

A thesis submitted to the faculty of
The University of Utah
in partial fulfillment of the requirements for the degree of

Master of Science

Department of Mining Engineering

The University of Utah

August 2011

The University of Utah Graduate School

STATEMENT OF THESIS APPROVAL

The thesis of **Anthony Michael LeBaron**

has been approved by the following supervisory committee members:

James Donovan	, Chair	**5/13/2011** Date Approved
M.K. McCarter	, Member	**5/13/2011** Date Approved
Paul Jewell	, Member	**5/13/2011** Date Approved

and by **Michael Nelson** , Chair of

the Department of **Mining Engineering**

and by Charles A. Wight, Dean of The Graduate School.

ABSTRACT

Blasting is a major expense and important part of many mining operations. Coal mines, metal mines, and quarries all use explosives as a tool to fragment rock. Since one blast can cost tens or even hundreds of thousands of dollars, it is imperative that the mine optimize its blast design to create the desired fragmentation. In that spirit, this project is an evaluation of the effect of rock bridges on fragmentation.

The project evaluated three blasts through an experimental approach. Parameters of blasts (burden, spacing, hole diameter, etc.) were obtained from mine operators. Three dimensional photoanalyses of highwalls were performed to determine in-situ properties of rocks. Photoanalyses of muckpiles were performed to determine blast fragmentation.

In order to assess the effect of bridges on fragmentation, two separate approaches were taken. One approach assessed the effect of bridges on comminution factor. The other approach entailed the comparison of results to a well-known empirical fragmentation model.

The only clear correlation of rock bridges and fragmentation was the ratio of bridge to joint length. A higher ratio of bridge to joint length resulted in finer fragmentation for each of these field experiments. No correlation between fragmentation and total length of bridges or length density of bridges was detected. It was therefore concluded that bridges only correlate to fragmentation when considered alongside length of joints.

TABLE OF CONTENTS

List of Tables

ACKNOWLEDGEMENTS

Rather than an individual effort, a master's thesis is an aggregate of effort, a vast accomplishment of not just me but of several people who have helped, prodded, and taught me along the way. To that end, I wish now to express my eternal gratitude and humbly thank a few people. I am grateful for the guidance of Dr. James Donovan, my exceptional advisor. I am also grateful for Dr. Kim McCarter, who taught me how to test rock in his lab equipment in addition to being on my committee. Dr. Paul Jewell also bestowed his presence upon my committee. Pam Hofmann, administrative assistant extroardinaire, helped me stay organized and afloat.

Several people helped my in my field and lab work to make this project possible. Kenny Thompson let me gather data from his mine. Bryson Hinkins of Staker Parsons inundated me with data from his operation.

I would be amiss not to thank a few other people. To my kind, loving and nurturing parents, Mike and Cindy LeBaron, thank you. I also want to thank my fellow graduate students for their support and friendship. Rock on.

CHAPTER 1

INTRODUCTION

Rock blasting is frequently used in mines and quarries to break large rocks in to smaller pieces. Smaller rock is easier to move and therefore more conducive to efficient operation. Furthermore, crushers designed to produce rock fragments of a certain size all have an optimal feed size and operation will run better with a blast that has been carefully designed to produce the desired fragmentation. Even though blasting is often the cheapest way to fragment rock (Persson et al. 1994), blasting can still cost mines millions of dollars per year. Therefore, it is always in a mine's or quarry's best financial interest to optimize blast fragmentation. Consequently, any information that can optimize blast design is potentially useful to the mining industry. It is with this in mind that this thesis investigates the effect of rock bridges on blast fragmentation.

Mineral production has historically been comprised of two steps: mining and processing. However, there has been recent interest in optimizing production by integrating the two processes. The integration of the two processes is known as mint-to-mill optimization (DOE 2006). Since processing relies on the output of the mine, the output of the mine should be optimized for the processing stage or the processing stage should be designed around the mine's output so that the whole project may be combined in to one process. Mine-to-mill optimization has the important benefits of increasing

throughput while reducing energy consumption and use of explosives.

When characterizing a rockmass, orientation and spacing of joints, and sometimes even persistence, are typically considered. However, discrete rock bridges are generally not recorded as part of a typical rockmass characterization program. A rock bridge is defined as the intact portion of rock between two fractures (Pariseau 2007). A rock bridge occupies a critical space during blasting as the nexus at which a joint will either continue to propagate or not. Hence rock bridges are of paramount importance in determining the fragmentation properties of a rockmass.

However, the effect of discrete rock bridges has been as of yet unexplored. In-situ size of rock blocks is often compared to muckpile block size distribution in order to calculate the comminution factor, or the ratio of postblast to preblast rock size.

Theory says that blasting tends to propagate along existing fractures rather than create new fractures. However, new fractures do occur within rock masses- this is why the comminution factor is always less than one. This project seeks to answer the following questions:

1) What effect do rock bridges have on fragmentation?
2) Can the effect of rock bridges be used to explain deviation from results predicted by other models of blast fragmentation?

As part of the project, three blasts were observed and documented. Two different experimental approaches are taken to investigate the effect, if any, that rock bridges have on fragmentation. The first approach looks at comminution factor as a function of various properties of the rock bridges. The second approach uses a well-known empirical model for blast fragmentation, and investigates what influence rock bridges may have on the deviation of actual results from those predicted by the model.

CHAPTER 2

LITERATURE REVIEW

This chapter contains a review of current literature related to topics relevant to the project, including blasting, geotechnical mapping, rockmass characterization techniques, and rock strength.

2.1 Geotechnical Mapping by Terrestrial Digital Photogrammetry

Geotechnical mapping is an important consideration when working with any fractured rockmass. Locations and properties of joints can significantly affect the overall strength of rock, and are an important consideration when working with any rock engineering project.

Traditionally, joint mapping has been accomplished by hand using a compass and measuring joint orientations over a section line or sample area of the rock face to be analyzed (Terzaghi 1965). This method is time consuming and places personnel in the path of potential rockfall. Resulting data are often incomplete due to the time required. (Donovan and LeBaron 2009). The 1980s saw the introduction of computer processing of digital photographs for rockmass characterization. Uses included calculation of rockmass rating, two dimensional (2D) orientation of joints, and nonphotogrammetric methods to find 3D orientation of joints (Franklin et al. 1988).

Recently, other methods for rockmass characterization have become popular, namely Light Detection And Ranging (LiDAR) and photogrammetry. LiDAR uses a laser pulse bounced off a rock face to detect distance from the source to the rock face. This process is repeated thousands of times to create a 3D "point cloud" that represents the rock surface. Typical laser scanners can collect 2,000-4,000 points per second at ranges up to 1 km (Donovan and LeBaron 2009). Setup in the field may take 15 minutes, with an additional 5 minutes to scan. Postprocessing takes less than 1 minute.

Digital terrestrial photogrammetry is also useful for rockmass characterization. Photogrammetry is the use of stereo pairs of photographic images to generate 3D models. By correlating known points between photos where the camera is at two known locations, physical locations of these points can be found.

One major drawback of photogrammetry is that control points are required to properly orient the image (ADAM 2010). While some laser scanners can be oriented directionally, a photogrammetry model requires at least three control points in the image. Setting up these control points usually requires the use of global positioning system (GPS) or a total station and can significantly increase the field time required to create a model from photogrammetry.

3DM Analyst, a 3D photogrammetry package produced by ADAM Technologies, uses stereo pairs of images to create 3D models. Six basic steps are required to make 3D models (ADAM 2010):

1) Camera calibration: Numerous photos of an object are taken with a given camera/lens combination. The software performs an adjustment to compensate for the effects of lens distortions, making locations accurate to 1/10 of a pixel.
2) Image Acquisition: Photo pairs are taken. Control points must be established.

Aperture and focus should be consistent between pairs of images (Birch 2006).

3) Establishment of location and orientation of cameras: Based on known location of control points (minimum of three), triangulation is performed to determine location and orientation of cameras.
4) View Images in 3DM Analyst: Thousands of points from both photos are correlated to each other, i.e. some point on a feature in the left photo is matched to a point on the right photo and this is repeated for thousands of points.
5) Creation of 3D coordinates: Based on position and orientation of cameras, correlated points are located by intersection.
6) 3D Data: 3D data are displayed and can be manipulated by the user.

Time spent in the field for photogrammetry can be as short as 2 minutes, but can be much longer if control points must be placed and surveyed. Image postprocessing takes 5 to 10 minutes on a modern computer. The camera and lens combination used must be calibrated which takes roughly an hour; however, this must be done only once for each camera/lens combination (Donovan and LeBaron 2009).

Both LiDAR and photogrammetry offer considerable advantage over traditional mapping in both time spent in the field and completeness of data. Photogrammetry records more points but there is no discernible advantage in the quality of the results (Donovan and LeBaron 2009). Photogrammetry can take less time in the field and the cost of equipment is lower, although the use of control points for image orientation can increase total time considerably. Discontinuity orientation data are arguably better than data gathered using a traditional clinometer because the come from measuring several points on a discontinuity surface. (Sturzenegger and Stead 2009)

Structural extrapolation requires assumptions about the character of the rockmass,

namely the assumption that certain regions are homogeneous. An extrapolation is valid only when it can be stated that similarities are probable. For example, the assumption can often be made that regions bounded by faults are structurally homogeneous but crossing a fault may change the nature of the rockmass.

LiDAR, photogrammetry, and traditional joint mapping are all subject to similar errors in a quarry or surface mine. Ideally, blasting leaves a smooth highwall in the pit. However, a flat planar structure will be less likely to be detected if it is oriented perpendicular to the plane of the highwall since the joint may appear as a linear feature rather than a plane (Terzaghi 1965). Photogrammetry can also be subject to orientation bias caused by occlusion. If the line of sight of the camera is steeper than a discontinuity, the discontinuity will not be detected (Sturzenegger and Stead 2009). Both occlusion and orientation bias are illustrated in Figure 1.

Scale and resolution in photogrammetry vary in a given 3D model (Sturzenegger and Stead 2009). Specifically,

$$S = \frac{f}{D} \tag{2.1}$$

where S is scale, f is focal length, and D is the range from camera to target (Figure 2). Since D may vary considerably over an image while f remains constant, it follows that S will vary as well.

The resolution on the ground or "ground pixel size" can be expressed as (ADAM Technology 2010):

$$PS_{ground} = \left(\frac{D}{f} \right) PS_{image} \tag{2.2}$$

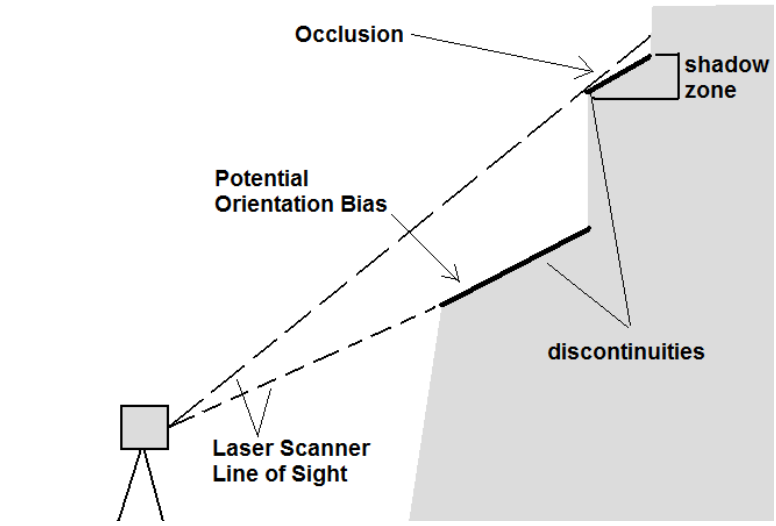

Figure 1: Illustration showing potential for orientation bias. After Sturzenegger and Stead (2009).

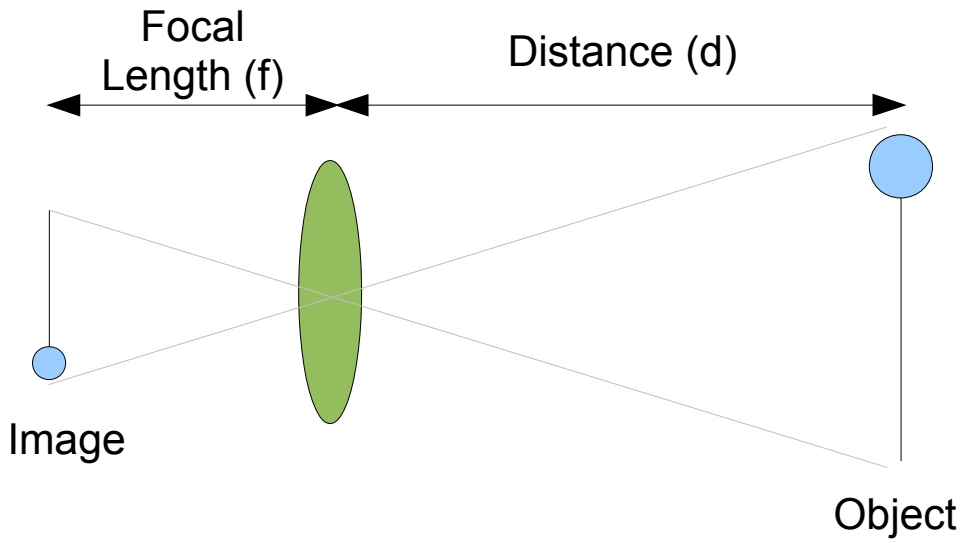

Figure 2: Light traveling from object to camera sensor. After ADAM (2010).

where PS is pixel size, measured as the linear dimension of one side of a square pixel. PS_{ground} refers to the amount of space on the ground represented by one pixel, where PS_{image} represents the size of one pixel on the camera's image sensor. PS_{image} can be calculated by dividing the length of the image sensor by its maximum resolution in that dimension. Usually, pixels are square so the same number will result regardless of which dimension is calculated. Again, ground pixel size will vary throughout an image.

Pixel size has a direct effect on the accuracy of the image. Accuracy consists of two descriptors- *planimetric* and *depth* accuracy (Birch 2006). Planimetric accuracy refers to the accuracy expected in a plane parallel to the camera's image plane, and is a function of quality of camera calibration and accuracy of control points. Planimetric accuracy can range from 0.05 pixel lengths to 0.5 pixel lengths (Birch 2006). Therefore, to ensure high planimetric accuracy, ground pixel size should be as small as is practical.

Depth accuracy is a function of distance from camera to pit wall, distance between camera stations, and planimetric accuracy (ADAM Technology 2010).

$$\sigma_{depth} = \frac{d}{b}\sigma_{planimetric} \tag{2.3}$$

where d is distance from camera to wall and b is the *base*, or distance between camera stations. The values of σ and b have an inverse relaitonship. Therefore, accuracy improves as b increases. It is worth noting that discontinuity orientation measurements are not affected by these accuracy metrics (Sturzenegger and Stead 2009).

Three dimensional data clouds are typically processed using a meshing technique. First, the point cloud (Figure 3) is covered with a triangular mesh. The mesh is oriented

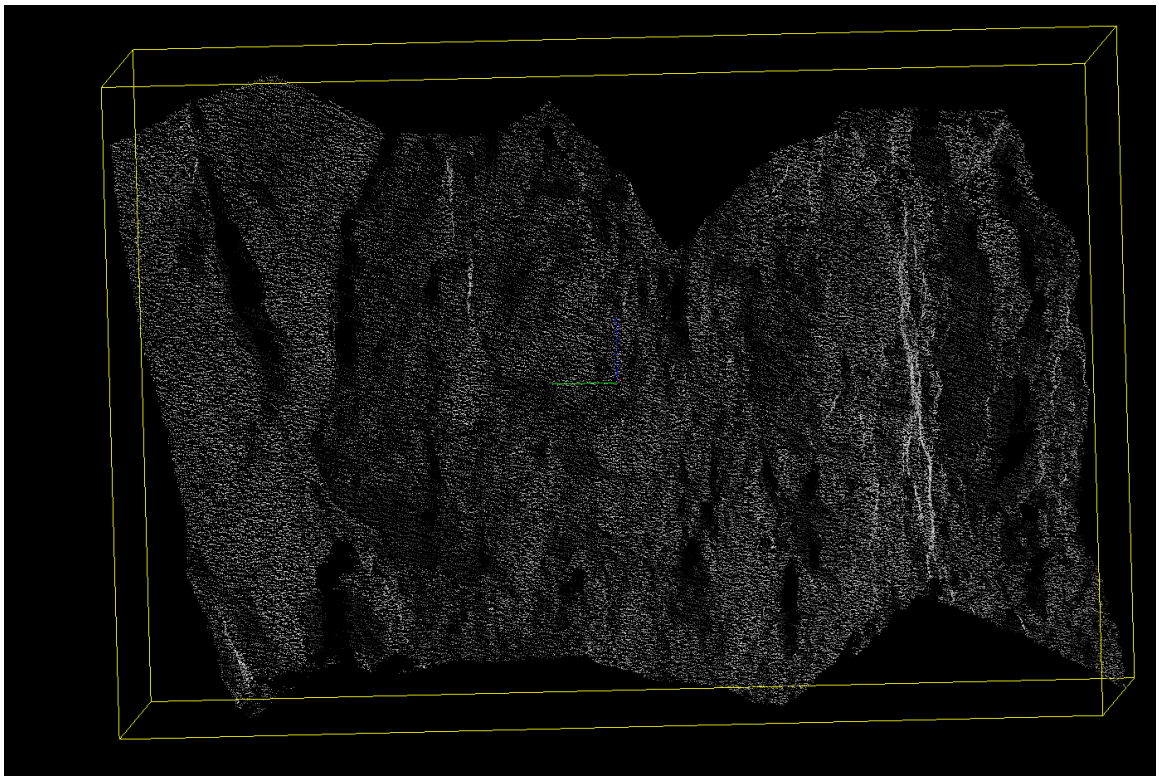

Figure 3: Example point cloud derived from photogrammetric data

perpendicular to the line of sight of the camera. Then, the centroid of each mesh triangle is placed at the mean location of the points enclosed by that triangle (Figure 4) (ADAM Technology 2010).

It is also possible to digitize a discontinuity surface from traces that may not appear as planar features. This is done by manually outlining the trace and fitting a plane through the points.

Like any joint survey, photogrammetry is prone to bias. First, joint sets that are nearly parallel to the face intersect the face less often, making them appear less abundant than they actually are (Terzaghi 1965). Joint spacing seen on a highwall or drill hole may be expressed as

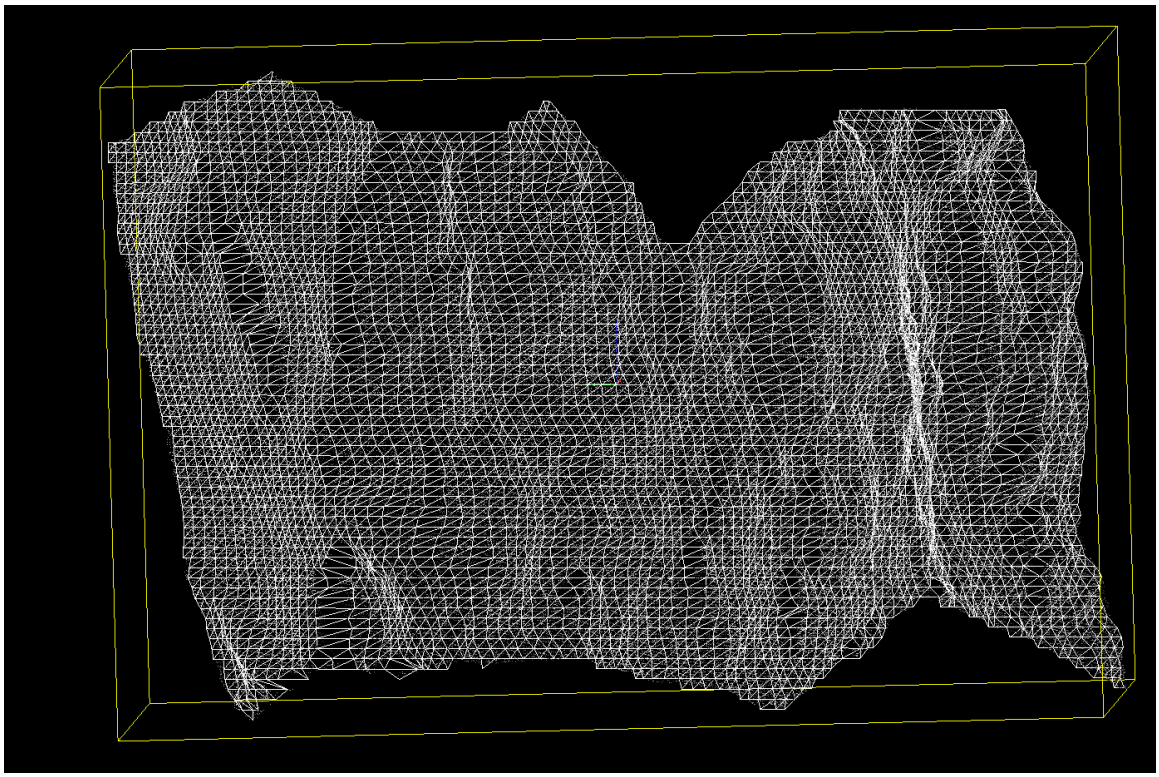

Figure 4: Example point cloud covered with triangular mesh

$$N_{\alpha} = \frac{L \sin \alpha}{d} \tag{2.4}$$

where Nα is the number of joints that appear in an exposure, L is the length of the exposure (in this case, height of the highwall if the highwall is vertical), d is spacing between joints, and α is the angle the joint makes with the highwall. This concept is illustrated in Figure 5.

2.2 Grouping Joints into Sets

Typically, joints are grouped into sets for engineering purposes. Traditionally, poles are plotted on a stereonet (Figure 6) and contours may be used to determine groupings of joint sets (Jimenez-Rodriguez and Sitar 2006). Contours are made based on

how many poles fall within a circle of arbitrary size (typically 1% of stereonet area) moved about the stereonet (Figure 7). However, this technique is prone to bias and indeed the size of the circle used can change results arbitrarily, making them meaningless (Harrison 1992).

A technique that has gained popularity is the use of k-means clustering, first introduced for use in rock by Harrison (1992). This method eliminates the sampling bias found in the counting circle approach. It groups poles in to "fuzzy sets," that is, each pole carries a certain probability of belonging to a given set by way of a "membership value." Fuzzy sets eliminate some of the bias produced using contouring (Harrison 1992).

One of the most popular algorithms using fuzzy sets is k-means clustering. In k-means clustering, membership values are assigned as a function of distance between poles, direction vectors, centroid coordinates, and an arbitrary weighting exponent q that controls the "fuzziness" of the sets.

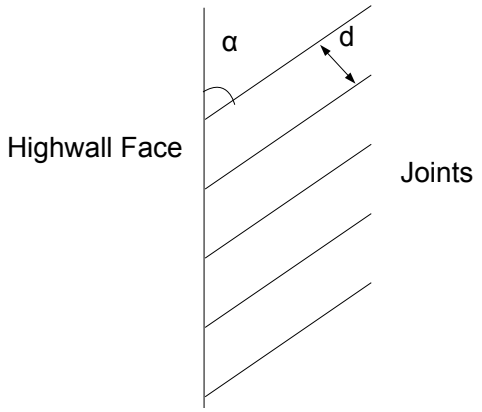

Figure 5: Joints intersecting highwall face

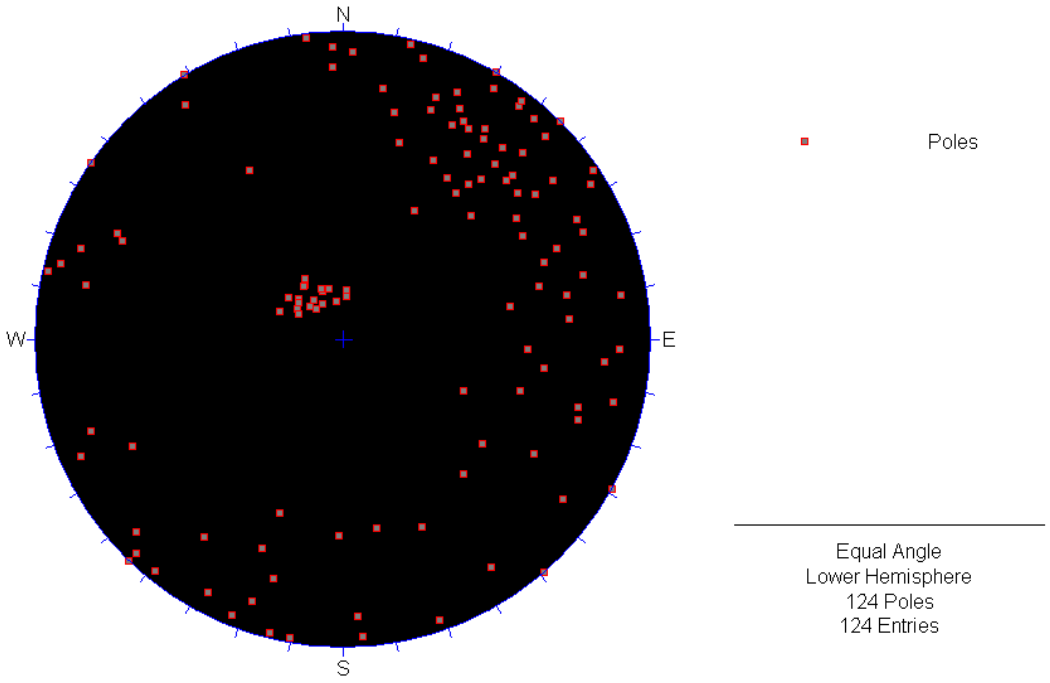

Figure 6: Poles plotted on a stereonet

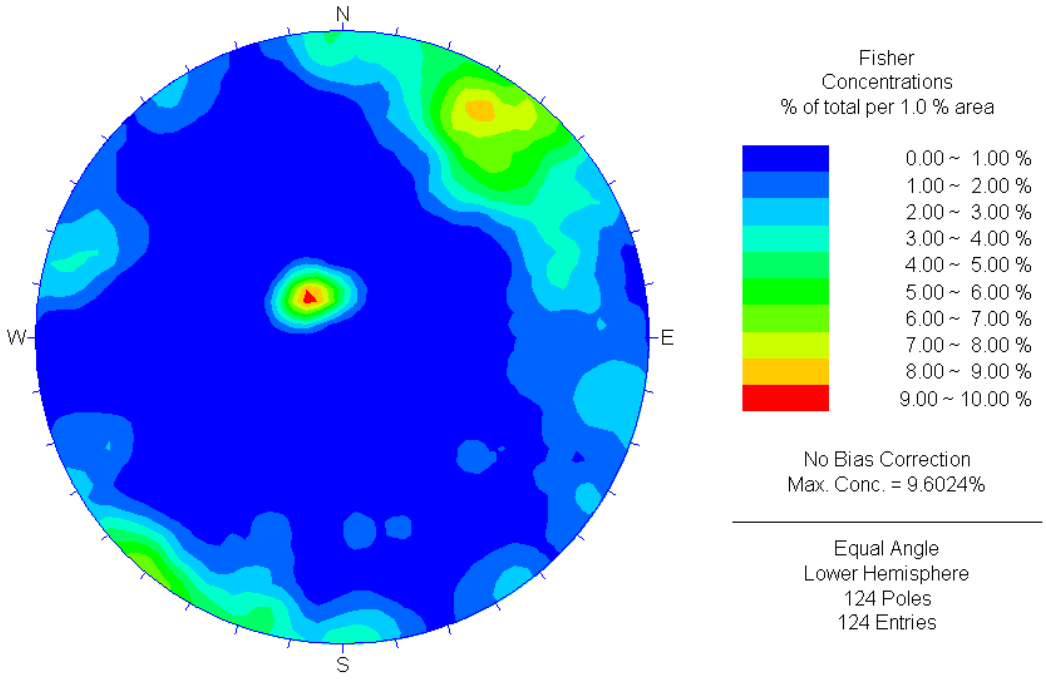

Figure 7: Contours based on 1% of area

2.3 Persistence and Rock Bridges

Rock joints are finite structures. Often in rock mechanics, joints are characterized using *persistence,* defined as the ratio of fracture area to total area in a single joint (Pariseau 2007).

$$p = \frac{A_j}{A} \tag{2.5}$$

Persistence is an important concept to use when looking at rockmass behavior influenced by joints. The mechanical difference between intact rock and joints is huge, so the inclusion of intact rock segments when calculating joint properties is significant (Gehl and Kutter 2003).

Shear failure in impersistent joints involves the shearing of both the fractured area and the bridge, or intact portion. This relationship is defined numerically as

$$\tau A = \tau_r A_r + \tau_j A_j \tag{2.6}$$

where τ_r and τ_j are shear strength of the rock and joint, respectively, and A_r and A_j are area of the rock and joint, respectively (Figure 8).

Investigations into the effect of impersistent joints on slope stability have been done (Pariseau et al. 2008) but tend to be computationally inefficient. Other analyses indicate that rock bridges play a significant role in supporting stability and since they are not accounted for in traditional analysis, mitigation measures are often overbuilt (Frayssines and Hantz 2009). A cascading failure of bridges where fractures coalesce at

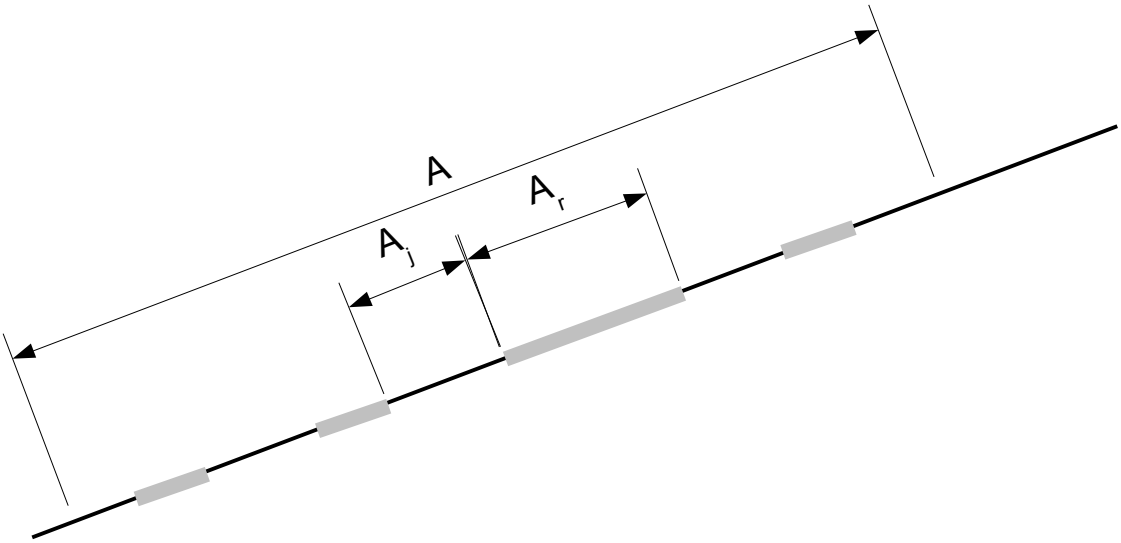

Figure 8: Effect of rock bridges on shear strength. After Pariseau (2008)

bridges and propagate through them is a step-path failure (Call and Nicholas 1978).

2.4 Rock Blasting

Blasting is frequently used in mining because it is an effective and inexpensive way to crush and sometimes move rock. Rock is drilled in a rectangular or staggered pattern (Figure 9), holes are loaded with explosives, and explosives are then detonated. Typically ANFO (Ammonium Nitrate- Fuel Oil) or an ANFO emulsion is used for blasting in surface mines. ANFO is an explosive mixture made of 94.5% ammonium nitrate prills and 5.5% fuel oil (Persson et al. 1994).

ANFO-based emulsions are also popular as they have the advantage of being water resistant and have a longer shelf life. An emulsifier can disperse a solution of AN in water into micron-scale droplets. The mixture still contains the explosive properties of ANFO but is water resistant since a thin film of oil around each droplet repels water

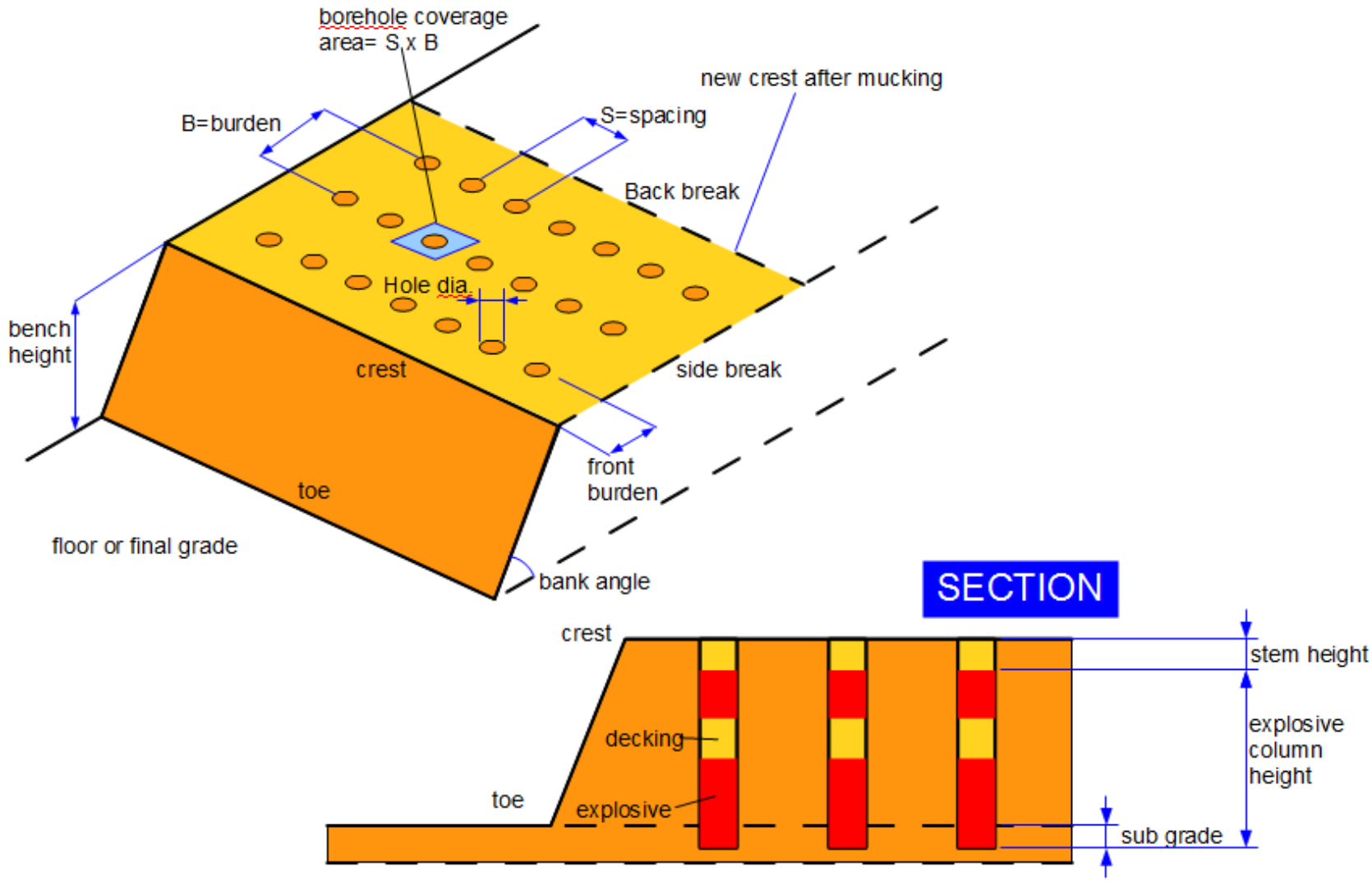

Figure 9: Design parameters in open pit blasts. After Goodquarry (2010)

(Persson et al. 1994). The water-resisting property has made emulsions extremely popular in mining applications where groundwater may be encountered.

2.5 Blasting Fragmentation

Many models exist to determine the distribution of rock fragment size distribution after blasting based on rockmass properties and explosive properties. Fragment size distribution is generally viewed as a percent passing curve, similar to a sieve analysis.

Kuznetsov (1973) proposed an empirical relation based on a "rock factor," volume of rock broken per blast hole, and TNT energy equivalent mass of explosive. The equation determines mean particle size. His equation is

$$x_m = A\left(\frac{V_0}{Q_e}\right)^{0.8} Q^{1/6} \tag{2.7}$$

where A = "rock factor" describing the blastability of the rock

V_0= rock volume per blast hole (Burden x spacing x bench height)

Q= mass of TNT equivalent to energy per blast hole

Rosin and Rammler (1933) proposed a formula for size distribution of coal particles based on a Weibull distribution, and their formula has since been widely adapted in the mining field for particles of any rock:

$$R = e^{-\left(\frac{x}{x_c}\right)^n} \tag{2.8}$$

where R=proportion of material retained on screen

x = screen size

x_c = characteristic size

n= index of uniformity

Cunningham (1983) combined Kuznetsov's empirical relation for mean size with the Rosin-Rammler formula for size distribution to produce the Kuz-Ram model for rock fragmentation size distribution. Kuznetsov's equation, rearranged to be more useful for explosives engineers, is (Cunningham, 1983):

$$\bar{x} = A\,K^{-0.8}\,Q_e^{1/6}\left(\frac{115}{E}\right)^{19/30} \tag{2.9}$$

where

K = powder factor (kg/m^3)

Qe = mass of explosive per blasthole

E = relative weight strength of explosive, where ANFO=100.

A = rock factor, an empirically derived constant accounting for strength of the rock.

Then, to calculate the index of uniformity for the Rosin-Rammler equation, the following equation was proposed:

$$n = \left(2.2 - 14\frac{B}{d}\right)\left(1 - \frac{W}{B}\right)\left(1 + \frac{(A-1)}{2}\right)\frac{L}{H} \tag{2.10}$$

where

B = Burden (m)

d = hole diameter (mm)

W = standard deviation of drilling accuracy (m)

A = spacing/burden ratio

L = charge length above grade level (m)

H = Bench height (m)

The procedure for calculating rock factor was later refined to be used based on rock mass characterization and mechanical properties of intact rock (Cunningham 1987).

$$A = 0.06(RMD + JF + RDI + HF) \tag{2.11}$$

where RMD is the *rock mass description*, JPS is based on vertical joint spacing, JPA is based on joint angle relative to highwall face, RDI is based on rock density, and HF is the hardness factor. JF is the sum of JPS and JPA (Table 1).

2.6 Strength of Intact Rock

Strength of intact rock is of critical importance to determining rock fragmentation. Many tests have been devised over the years, and they may be divided in to two categories: index tests and strength tests. Strength tests directly measure some fundamental mechanical property of a rock- compressive strength, tensile strength, or shear strength, for example. Results from an index test, while still useful, do not provide a fundamental property of rock and can be compared only to results of other index tests. Generally, index test results are applied through empirical formulas. While strength testsmay offer a more universally usable result, index tests are often quick to do and can

Table 1: Parameters for Kuz-Ram model. After Gheibe et al. (2009).

RMD		**Rockmass Description**
Powdery/Friable		10
Vertically Jointed		JF*
Massive		50
JPS		**Vertical Joint Spacing**
<0.1m		10
0.1m to MS		20
MS* to DP*		50
JPA		**Joint Plane Angle**
Dip out of face		20
Strike perpendicular to face		30
Dip into face		40
RDI		**Rock Density Influence**
RDI = 25 RD* -50		RD= rock density (t/m^3)
HF		**Hardness Factor (GPa)**
Y/3		if Y<50
UCS*/5		if Y>50
MEANING		**Unit**
MS	Oversize	m
DP	Drilling Pattern Size	m
Y	Young's Modulus	GPa
UCS	Uniaxial Compressive Strength	MPa
JF = JPS + JPA		

be easily deployed to a field site.

Rock strength is often defined more completely using failure envelopes based on the 2D major and minor principal stresses. The state of stress applied to an object may be described using a tool known as Mohr's Circle, shown in Figure 10. The circle is a visual aid used to represent shear and normal stresses on a plane of any given orientation. It is drawn with normal stress along the abcissa and shear stress along the ordinate. The major and minor principal stresses fall on the abscissa and represent two endpoints of a diameter of the circle. Thus, the circle's midpoint falls halfway between the principal stresses, and the radius is one half the difference between σ_1 and σ_3.

Failure in rock can be defined graphically using Mohr's circle. The rock is considered to have failed when its Mohr circle touches a line known as the failure envelope. Several different methods have been proposed to define the failure envelope. Probably the most common is the Mohr-Coulomb criterion, defined for the σ-τ plane in Eq. (2.12), where ϕ is the angle of internal friction and c is the cohesion.

$$|\tau| = \sigma \tan(\phi) + c \tag{2.12}$$

A different line may also be used to define the Mohr-Coulomb criterion, one that passes through the tops of the circles and is defined by the principal stresses. It returns the same failure results as Eq (2.11), but is stated in a different way in Eq. (2.13).

$$\tau_{max} = \sigma_{mean} \tan(\psi) + k \tag{2.13}$$

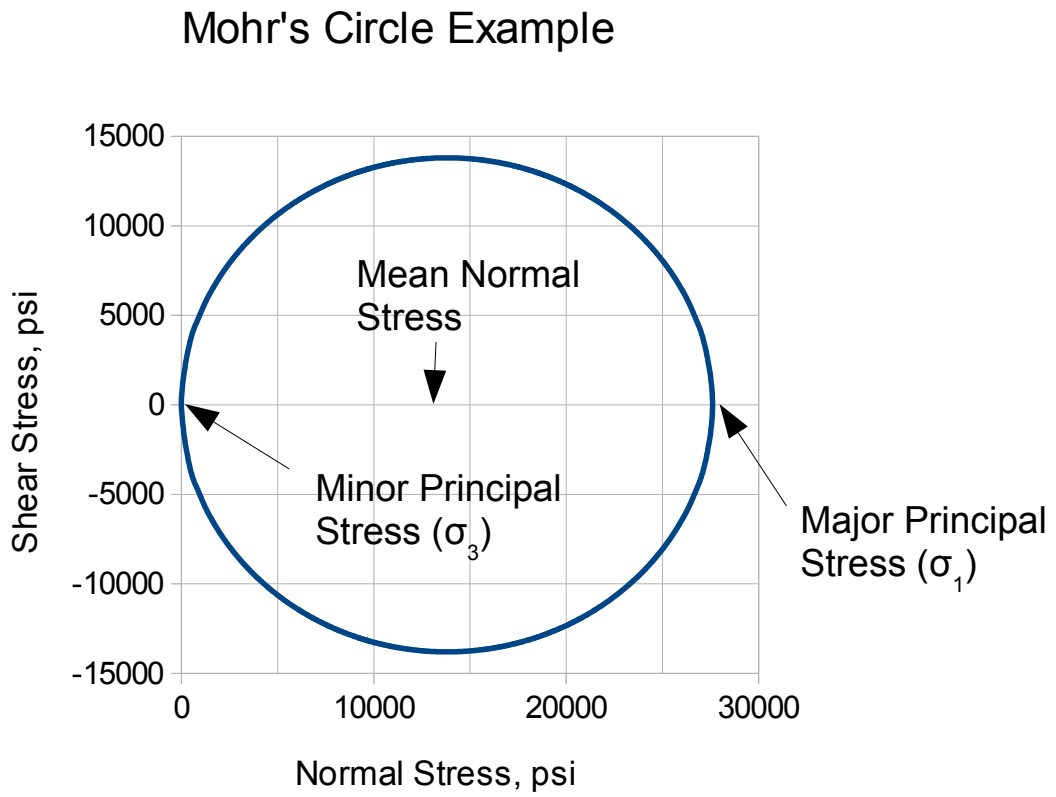

Figure 10: Example Mohr's circle for rock in uniaxial compression

Another popular failure envelope is defined by the Hoek-Brown criterion. The failure criterion is defined as

$$\sigma_1 = \sigma_3 + \sqrt{a\,\sigma_3 + b^2} \tag{2.14}$$

where a and b are determined experimentally. When rearranged for plotting on a shear stress-normal stress diagram for use with a Mohr's circle, the criterion becomes

$$\tau_m = -\frac{a}{2} + \frac{1}{2}\sqrt{a^2 + 4\,(a\,\sigma_m + b^2)} \tag{2.15}$$

which defines a parabola.

2.7 Strength Tests

The most commonly used strength test is unconfined compressive strength (UCS) (Pariseau, 2007). The setup is relatively simple- a cylindrical core of rock is put under axial compression until brittle failure is initiated. UCS is simply defined as force at failure divided by cross-sectional area.

In order to provide a more complete data set to define the failure envelope, triaxial tests are often used in addition to uniaxial compression strength. In a triaxial test, a core of rock is exposed to axial compression while simultaneously subject to constant confining pressure. Confining pressure is typically provided by a hydraulic sleeve. (Figure 11). Spherical seats ensure that load is directed axially and edge loading is not a concern. Strain gauges may be used if desired to determine Poisson's ratio and elastic modulus.

Less commonly, tensile strength may be measured directly. Direct tensile testing can be accomplished using a cylindrical core epoxied into a testing apparatus (Hoek and Brown 1980) as shown in Figure 12, but is usually avoided because of technical difficulties including end attachment and the brittle nature of rock in tension. (Pariseau 2007).

The Brazil test is an indirect method for determining tensile strength. It is often favored due to its low cost and simplicity. The Brazil test compresses a disk of rock diametrically (Figure 13). Ideally, compression induces high tensile forces along the diameter of the disk and causes a straight, clean tension crack. A setup is pictured in Figure 14. I The formula to convert critical load to tensile strength is given in Eq. (2.16).

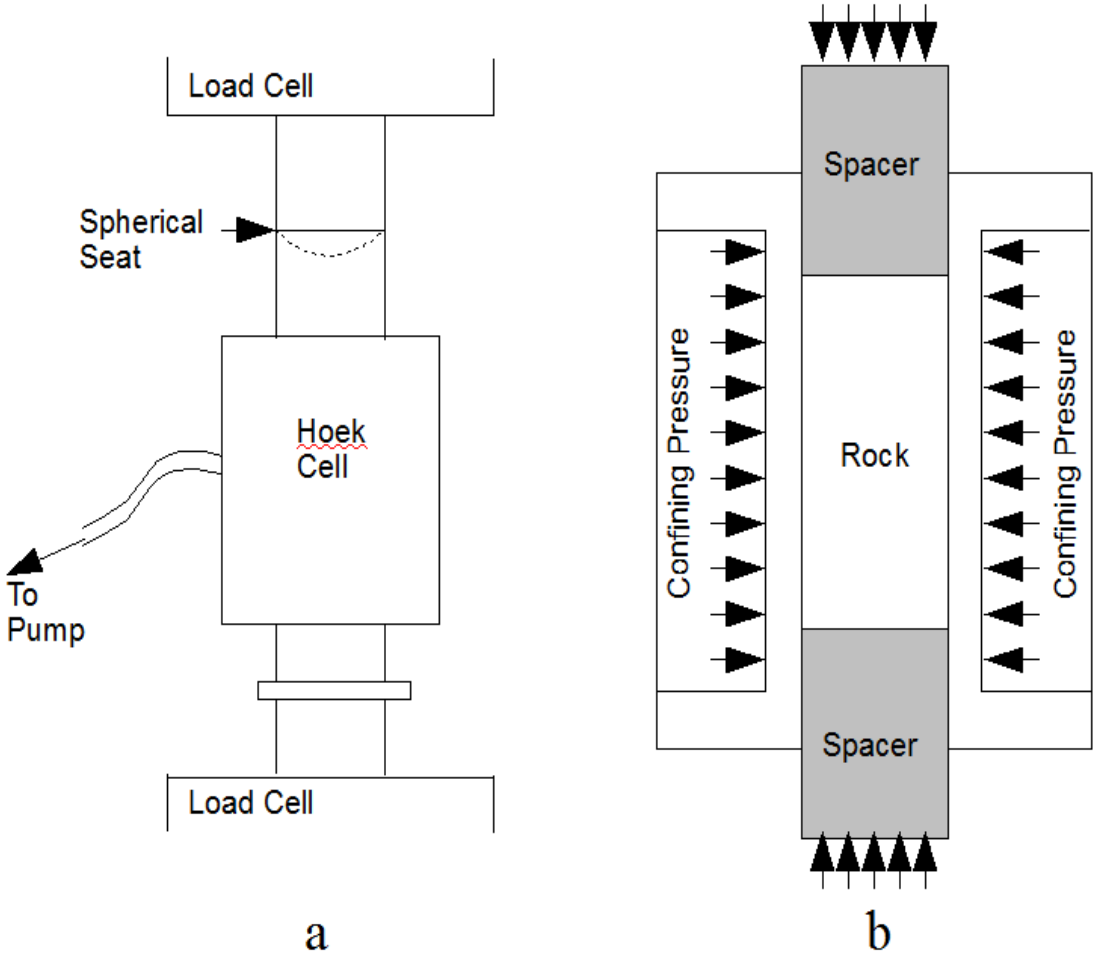

Figure 11: Illustration of testing setup (a) with cross-section view of Hoek cell (b)

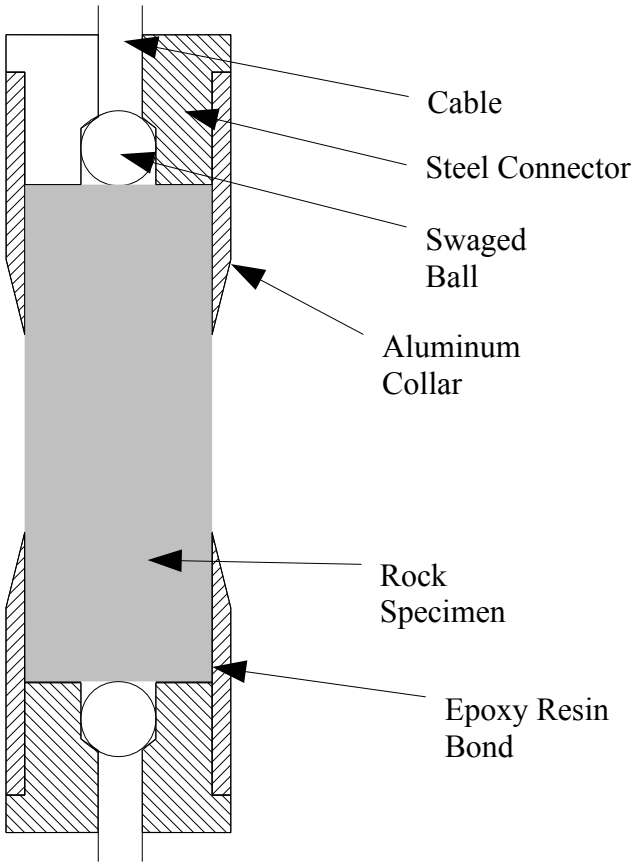

Figure 12: A setup for direct measurement of tensile strength. After Hoek and Brown (1980).

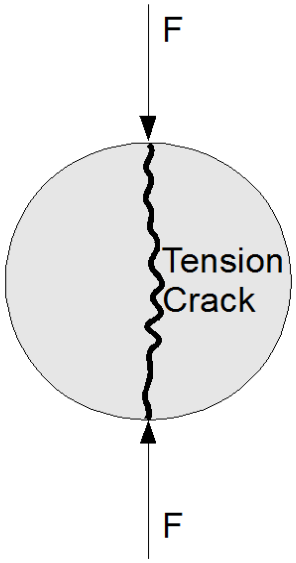

Figure 13: Ideal outcome of Brazilian Test

Figure 14: Sample being subjected to Brazilian test.

$$T_o = \frac{2F_c}{\pi D h} \tag{2.16}$$

F_c is the force at failure, D is the diameter, and h is the disk thickness (Pariseau 2007).

Another useful index test is the point load test, also known as the irregular lump test. The point load test can be easily deployed in the field and provides a useful strength index. First proposed by Hiramatsu and Oka (1966), the point load test places a rock of irregular shape between two concentrated loads. Their tests showed that if an object is loaded between two points, the stress state within is similar in the region between the two points regardless of shape. Therefore, a rock of any shape may be used for the point load

test (Hiramatsu and Oka 1966). The proposed equation is:

$$T = \frac{0.9\mathrm{P}}{D^2} \tag{2.17}$$

where P is critical load, D is distance between loading points, and T is tensile strength.

A point load test can be carried out on rock of any shape, so it is appealing in that no sample preparation is required. Furthermore, a small testing machine can be easily deployed to the field. The load should be applied by a platen with a tip of 5mm radius and a 60º angle (ISRM 1985). A platen is shown in Figure 15.

Although there is no standard sample shape for the point load test, there are certain requirements for dimensions and different calculations for different shapes. (ISRM 1985) The test can be divided into three subcategories: The diametral test, in which the load is applied across the diameter of a disc or core, the axial test, where load is applied down the long axis of a cylinder, the block test, where load is applied across a rectangular block, and the irregular lump test, where load is applied across a lump of irregularly shaped rock. These testing configurations are sketched in Figure 16.

Certain shape restrictions apply (Figure 17). In the case of a diametrically loaded test, the length of the cylinder must be greater than 0.5 times the diameter. For an axial test, the length of the core must be between 0.3 and 1 time the width of the core. For a block test, distance between loading points must be between 0.3 and 1 time width, and the block must be at least as wide as the distance between points.

The point load test result, which approximates tensile strength, is calculated from the following equations:

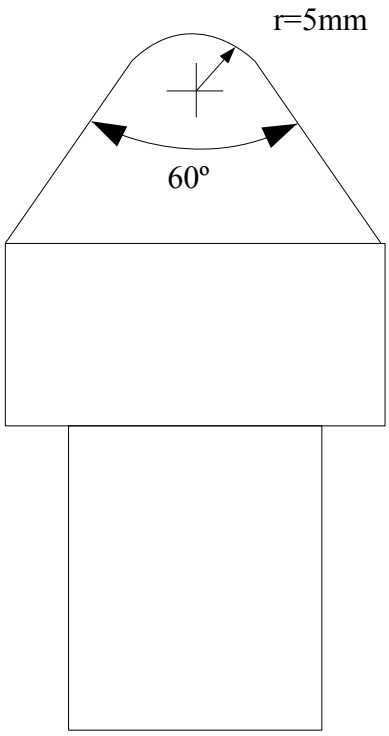

Figure 15: Standard platen for point load test. After ISRM (1985).

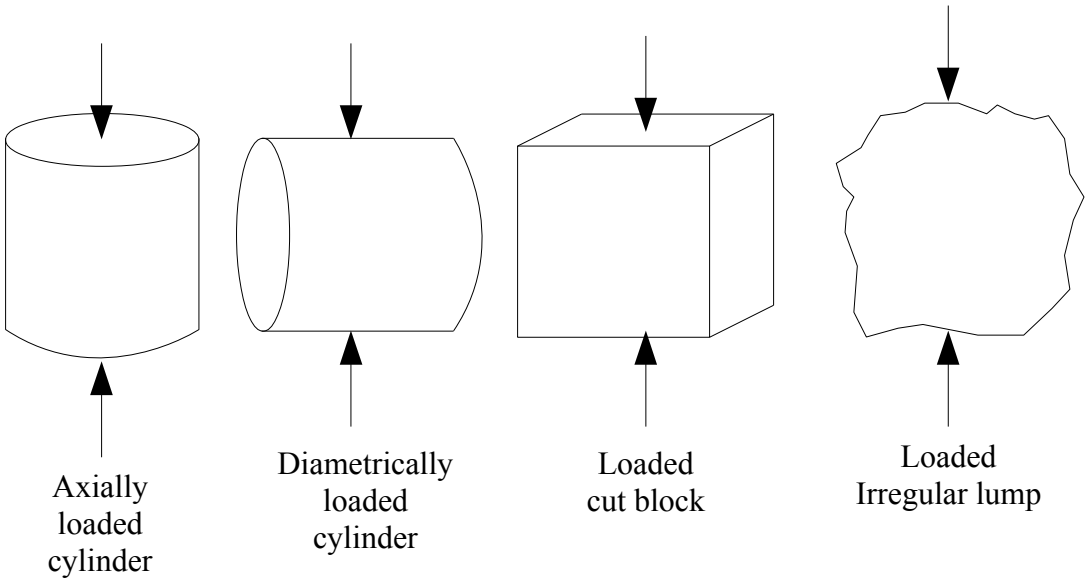

Figure 16: Point load testing configurations. After Russell and Wood (2009).

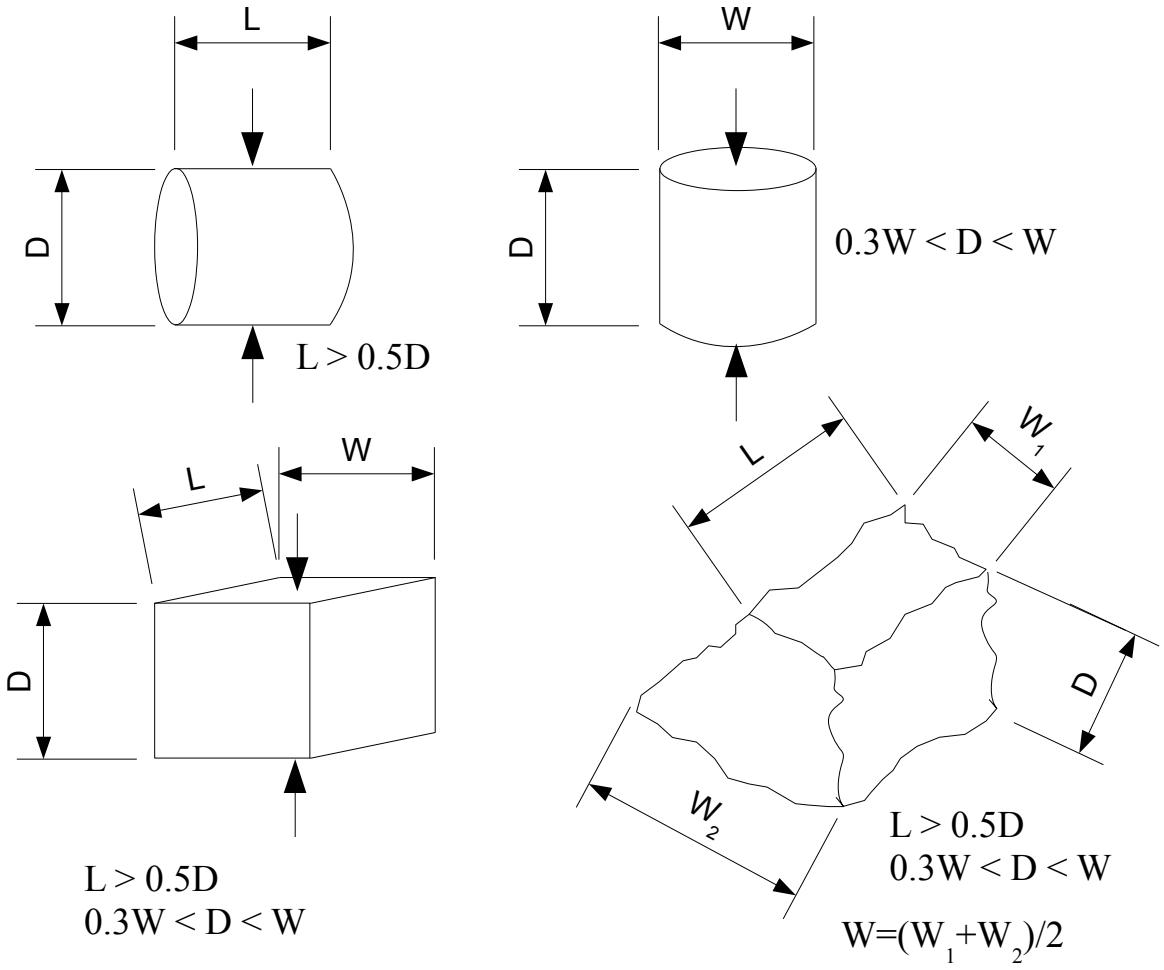

Figure 17: Dimensional restrictions for point load test. (After ISRM 1985)

For diametral tests:

$$I_s = P / D^2 \tag{2.18}$$

where P is load and D is core diameter. For axial, block, and lump tests, the uncorrected point load strength is:

$$I_s = P\frac{\pi}{4A} \tag{2.19}$$

where A is minimum cross-sectional area of a plane through the specimen between loading points.

The Schmidt Hammer test was originally developed by Swiss engineer Ernst Schmidt for nondestructive testing of concrete. The device uses a spring loaded hammer to strike the concrete surface, then measures the distance the hammer rebounds. Schmidt (1951) showed a strong linear correlation between hammer rebound percent and compressive strength of concrete.

More recently, Schmidt Hammer tests have been used with rock to determine UCS and elastic modulus. Currently, the ISRM recommends the hammer be placed within 5 degrees of perpendicular to the rock surface. Samples should be NX size core clamped to a steel base plate weighing 20 to 40 kg, depending on hammer size (Aydin 2008). At least 20 measurements should be taken.

Several empirical correlations between Schmidt Hammer tests and mechanical properties have been proposed. A comprehensive study by Katz et al. (2000) suggests the following equations for elastic modulus and uniaxial compressive strength, respectively:

$$UCS = 2.208\, e^{0.067\mathrm{R}} \tag{2.20}$$

$$E = 0.00013\mathrm{R}^{3.09074} \tag{2.21}$$

2.8 Rock Bridges And Blasting

A search of the literature reveals that nobody has ever explicitly investigated the effect of the presence of rock bridges on blasting fragmentation. Some numerical models take a synthetic rockmass (SRM) approach (Ivars et al. 2011), which is similar in that it looks explicitly at individual rock fractures. The SRM approach to numerical modeling involves 3D modeling of a rockmass with discrete joints or spaced joint sets added to the rockmass, which can simulate the presence of in-situ blocks.

CHAPTER 3

BACKGROUND AND JUSTIFICATION

In blasting, properties of a rockmass have a huge effect on the fragment distribution produced. While blasting models may account for joint orientation and spacing, none account for the effect of rock bridges. A rock bridge, however, could be a significant factor affecting blasting. A rock bridge is the nexus at which a fracture may either propagate or not. However, short of explicit rockmass modeling in numerical models, rock bridges tend not to be explicitly accounted for in blasting. Therefore it was thought prudent to explore the effect of rock bridges on blast fragmentation, specifically in relation to in-situ block size.

Rock fracture patterns are often idealized as systems of joints and bridges with a given persistence (Figure 18). The gaps in these joints, the bridges, can be filled in. Once filled in, the joints suggest an in-situ block size (Figure 19).

One way in which to explore the effect of rock bridges is through the comminution factor. Although it can be defined in a few different ways, in this paper comminution factor will be taken to be

$$F = \frac{A_b}{A_i} \tag{3.1}$$

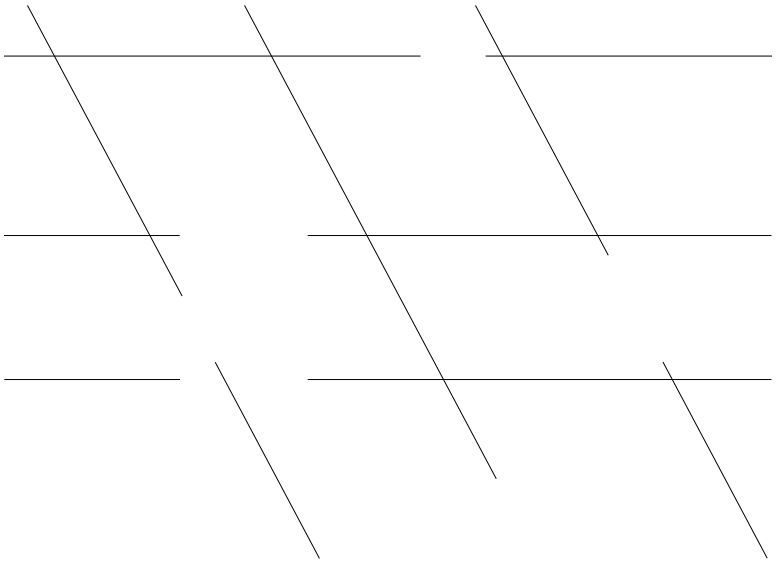

Figure 18: Idealized drawing of impersistent rock joints

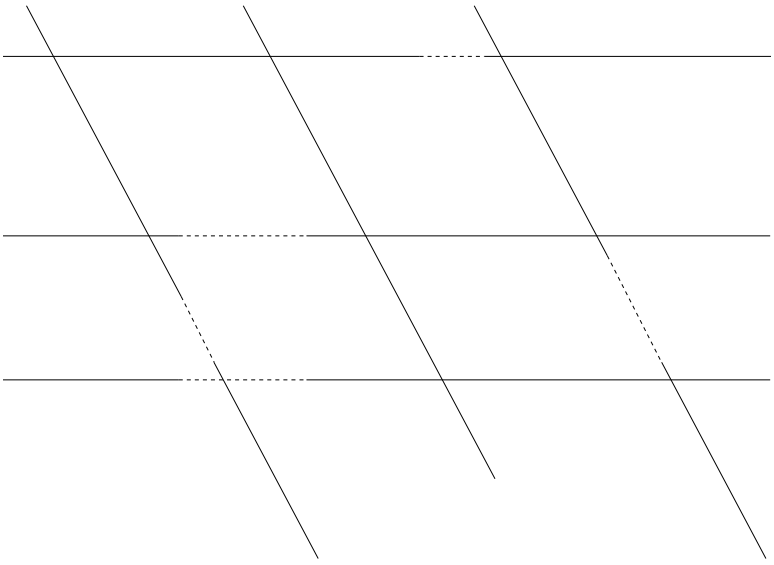

Figure 19: Idealized rock joints with bridges filled in, showing in-situ blocks

where

A_b = mean area (2D) of blasted rock particles

A_i = mean area (2D) of rock blocks in-situ

Comminution factor is a convenient way to look at fragmentation because it is a direct before-after comparison of block size. Furthermore, it is a convenient number to obtain in this project since extensive rockmass characterization was already being performed with respect to the delineation of joints. In a geomechanical context, using the comminution factor is reasonable because it is a ratio and therefore eliminates the effect of block size. Then the research can be more focused on the joints and bridges themselves.

A popular empirical blasting model was used as well to examine the effects of rock bridges. Obviously, no model is perfect and there must be some reason that reality deviates from the model. Ideally, a simple blasting model should account for intact rock properties, explosive energy, and rockmass/joint properties. Then, it should be presumed that any explosive energy goes into plastic deformation of rock and fracturing. However, blasting is not that simple in reality. Therefore, an empirical model was deemed appropriate for the project.

The Kuz-Ram model was chosen because it is popular, well-established, and accounts for all common factors that affect blasting: blast geometry, rock strength, and rockmass characterization. However, it does not account for rock bridges or joint persistence. Therefore it was deemed an appropriate model to examine the effects of rock bridges, with the hope that deviation between the real world results and results predicted by Kuz-Ram would have a relationship to the properties of rock bridges.

Although only three blasts were observed, the use of two tests (comminution

factor and Kuz-Ram model) will produce a more rigorous examination of the effects that bridges have on fragmentation. If a trend or correlation is shown to appear in one test but not the other, with only three data points, it may not be clear if that is a true trend or just a statistical anomaly. However, if similar trends manifest in both the Kuz-Ram and comminution factor comparisons, the confidence in those trends increases.

CHAPTER 4

EXPERIMENTAL PROCEDURE

Chapter 4 outlines the locations of field work, field procedures, experimental procedures, lab work, and postprocessing.

4.1 Description of Field Sites and Blast Locations

Three blasts were documented for the project.

The first blast was at Staker-Parson's Beck Street quarry in Salt Lake City (Figures 20, 21). The quarry produces aggregate for concrete. The blast occurred in a highly fragmented limestone with heavy jointing and dense veins.

The other two blasts were at Western Gypsum's surface mine in northern Arizona, immediately south of St. George, UT (Figures 22, 23). One blast was in a massive, blocky limestone overburden material that was treated as waste rock. The other blast at the gypsum mine was in the gypsum ore, which was destined for the mine's crusher.

All three blasts were intended only for fragmentation, not to move the rock. All three blasts were drilled with 6.75” holes, no subgrade drilling, and a small amount of stemming. All blasts were arranged in square patterns. Furthermore, all three blasts were in sedimentary rock. Given all the similarities between these three blasts, it is reasonable to suppose that any significant differences in fragmentation will be due to the properties

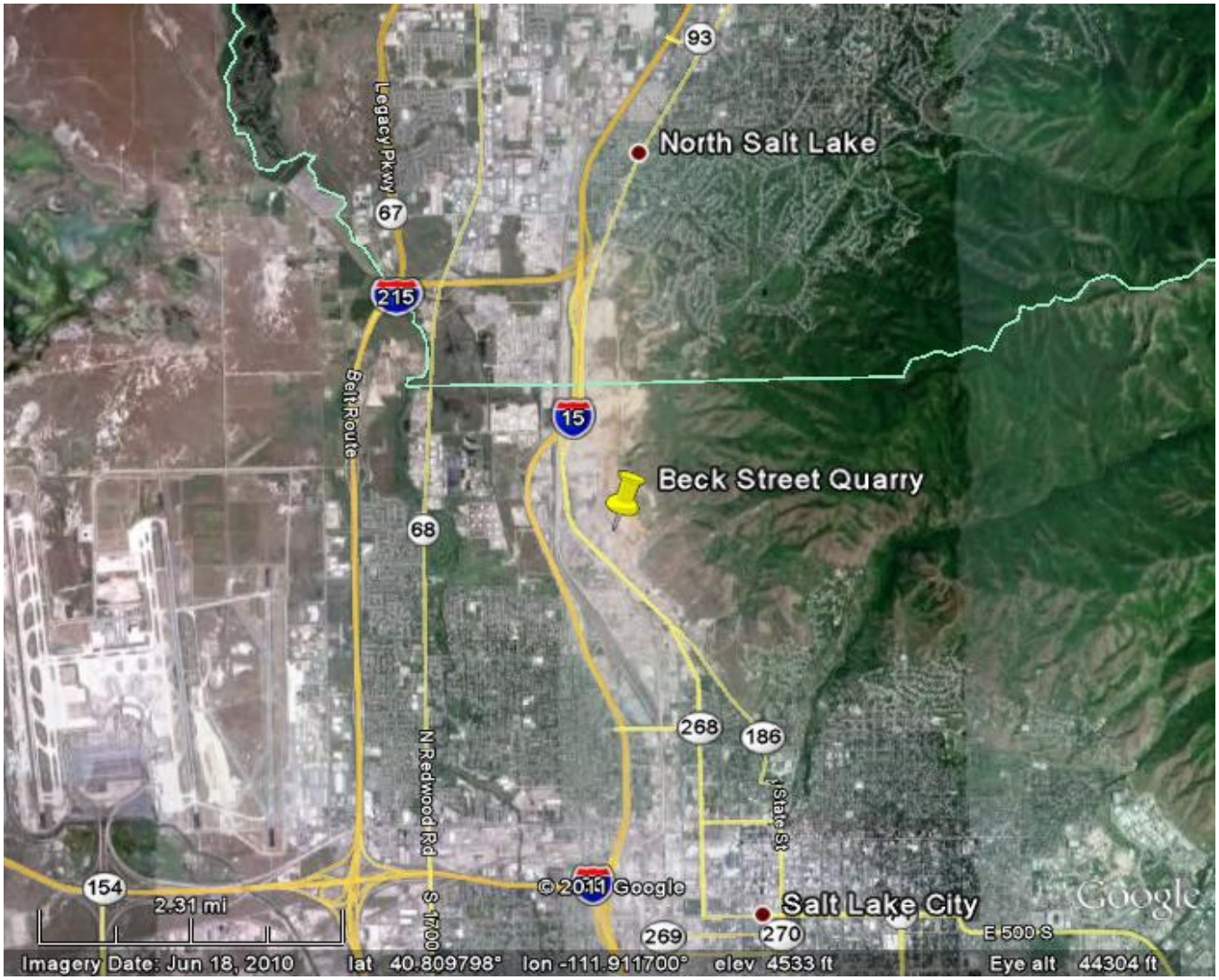

Figure 20: Location of Beck Street Quarry. (Photo: Google)

Figure 21: Aerial photo showing location of blast within quarry (Photo: Google)

Figure 22: Aerial photo showing location of gypsum mine. (Photo: Google)

Figure 23: Aerial photo showing location of blasts within gypsum mine. (Photo: Google)

of the rock. As such, these three blasts represent an excellent opportunity to examine the effect of rock structure on fragmentation.

4.2 Field Procedure

4.2.1 Safety

Safety was of primary concern in this project. Several hazards were present: large equipment was often working in the area, rockfall was a constant threat, and explosives were often present. Equipment operators were notified of the team's presence in the area before entering. To mitigate risk, the team stayed back from the highwall when on top in case of sudden or human-triggered instability. When below the slope, the team stayed far away from the highwall due to the ever present hazard of rockfall. Necessary personal protective equipment (PPE), including hard hats, reflective vests and safety shoes, was worn at all times while in the field. During times when blasts were observed, recommendations of the mine operator were followed for staying a safe distance away to avoid any of the hazards associated with blasting, including flyrock and noxious gases.

4.2.2 Control Point Setup

Circular targets were surveyed in for high accuracy using differential GPS with the help of the mine surveyor. About six targets were used for each scene. Generally, three targets were set up at the crest of the highwall, and three were set up on the pit floor near the highwall but far enough away to keep the surveyor out of the path of potential rockfall. Every attempt was made to space control points evenly; however, sometimes obstacles such as slope geometry or hard ground made it impossible or unsafe to put a control point in the desired location. In these cases, targets were placed wherever

possible. Figure 24 serves as an example of nonideal target placement. Note that two control points at the toe of the slope are somewhat close together. To the left, the ground was hard and stakes could not be driven in and so the left-most stake is further right than desired.

4.2.3 Photography

Photographs were taken using a Nikon D200 digital SLR camera. Photographs have a resolution of 3872x2592 pixels. A lens with 60mm focal length was used. A high F-stop number was generally preferred (usually f/10), as the narrow aperture gives photos

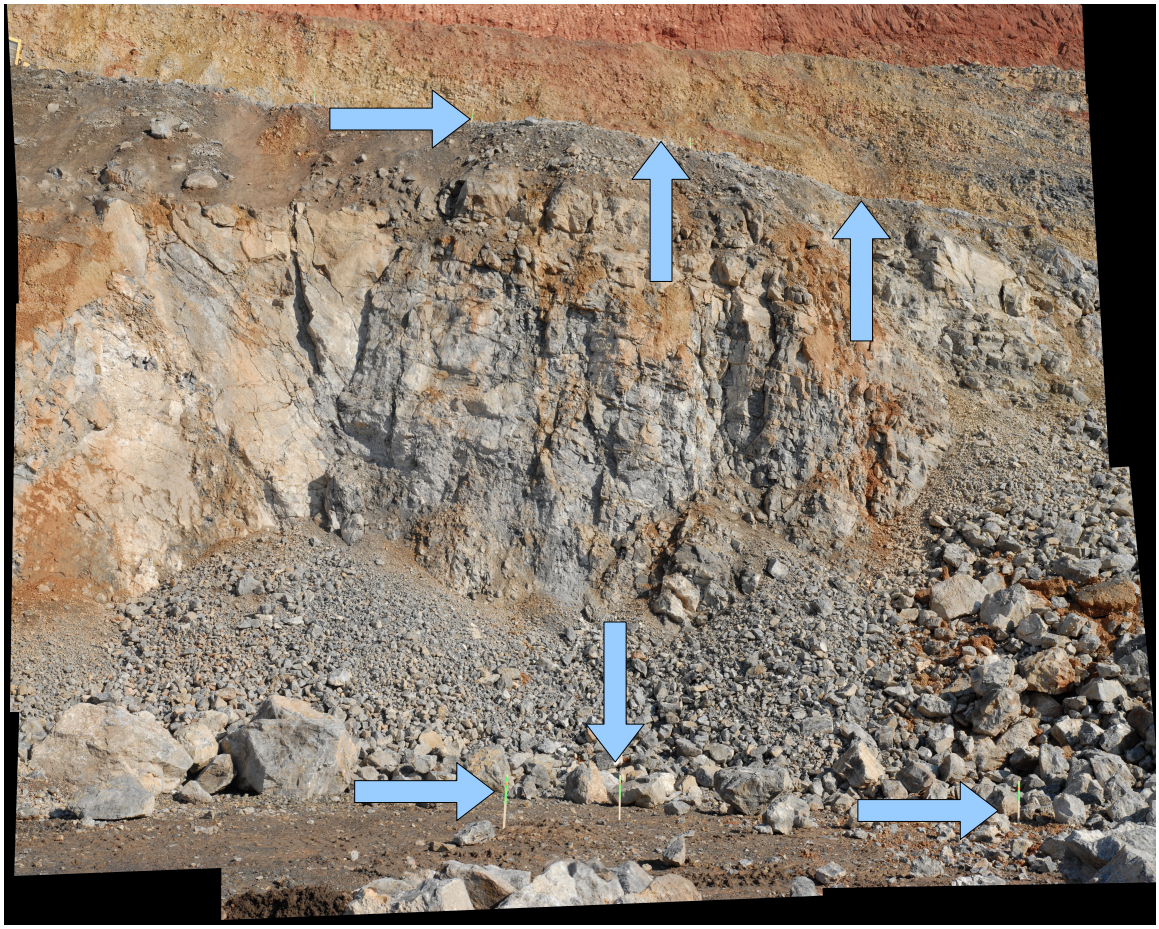

Figure 24: Sample photo showing control point locations in Beck St. quarry

a greater range of depth, meaning more of the photo is sharply in focus. Having the photo sharply focused aids 3DM analyst in identifying common points.. Focus ring on the lens was taped manually as recommended by ADAM (2010) to maintain consistent focus.

The camera was attached to a tripod in order to eliminate motion blur in photos. Photos were taken in a fan configuration to allow later mosaicking in 3DM CalibCam. This way, even with camera resolution limited to 10 megapixels, a final photo mosaic from one station can have around 50 megapixels. Ideally, the distance between camera stations was one tenth the distance from the camera to the highwall, as recommended by ADAM (2010). An ideal camera setup is illustrated in Figure 25. The camera was moved to three or four stations at each site, and the best pair of mosaics (Figure 26) was used in 3DM Analyst. The “best” pair was that with the best balance of residuals.

4.3 Postblast Particle Size Analysis

Particle size distribution of blasted rock was calculated using digital photographic analysis. The software package Split Desktop by Split Engineering was used. Two objects were used for scale in each photo- spherical objects (in this case, soccer balls) were preferred as they have the same apparent diameter regardless of viewing angle (Figure 28).

Photos were first analyzed using Split's default settings, and settings were tweaked until the software was able to identify particle size to a satisfactory degree of accuracy. Then, manual delineations were made as needed in order to have an accurate representation of fragment size.

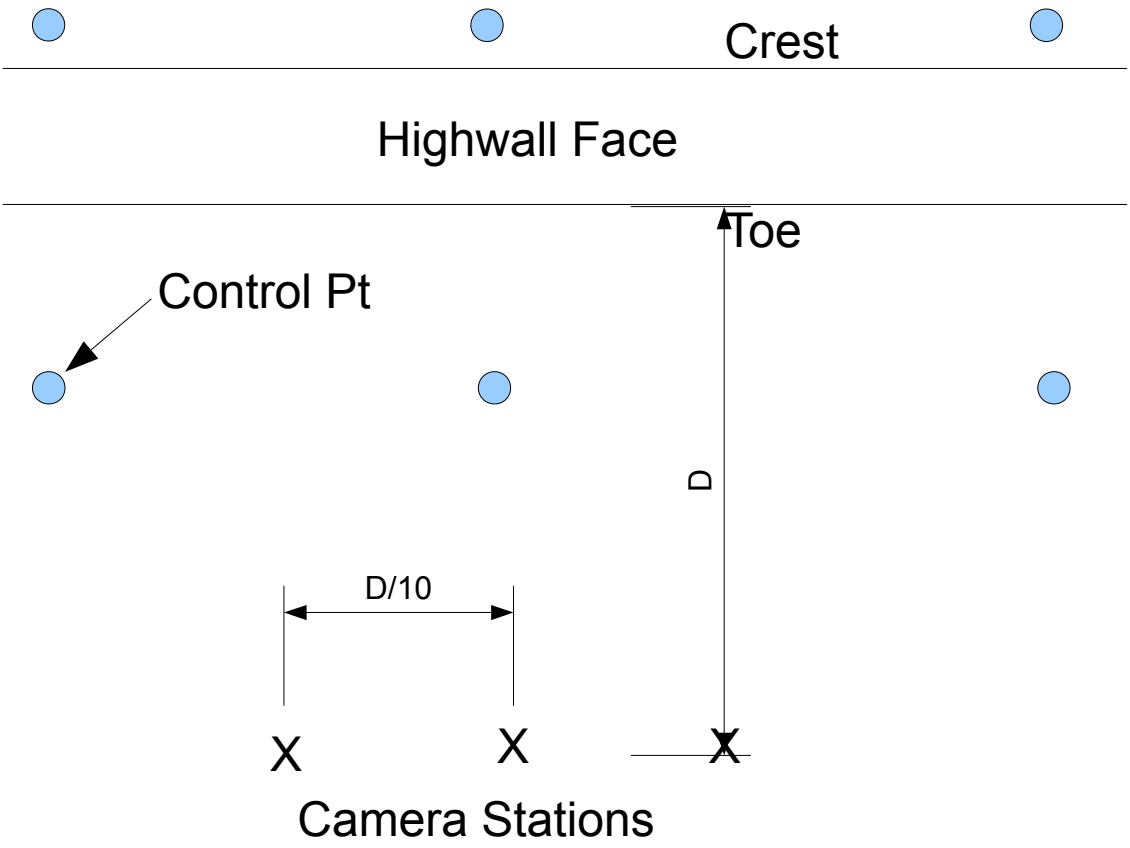

Figure 25: Plan view of ideal field layout for photogrammetric analysis

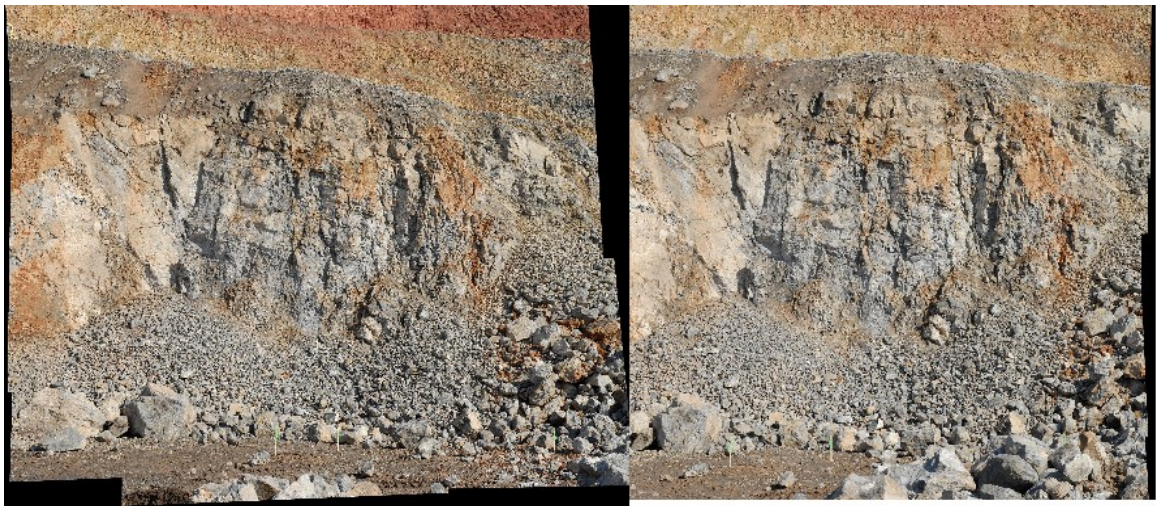

Figure 26: Left and right images forming an image pair

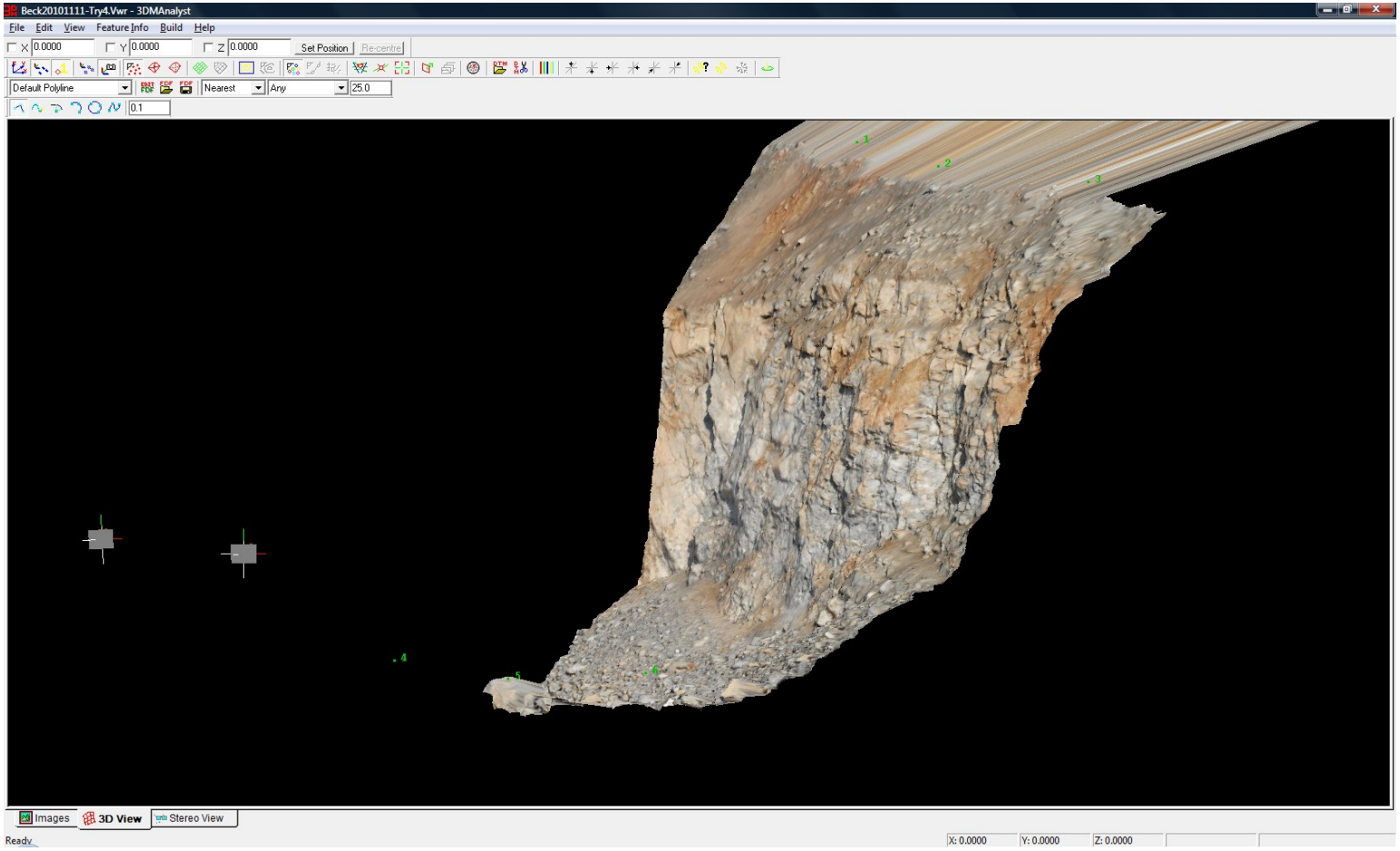

Figure 27: 3D model made from images shown in Figure 26

Figure 28: Muckpile photo with balls for scale

4.4 Rock Testing

4.4.1 Rock Sample Preparation

For this project, both tensile and compressive strength were obtained. Rocks from all three sites were tested. Unconfined compressive strength (UCS) was measured using AX size (32mm diameter) cores in the University of Utah's rock mechanics lab. Tensile strength was measured using the Brazil test, also on AX core.

Since rock samples gathered for testing were small, they were first cast in concrete using particle board forms. The purpose of the forms was to:

1) Add weight to hold rocks still during drilling
2) Create a rectangular shape, allowing samples to be clamped into a vise for stability while drilling (Figure 29).

AX size core was used. Although a larger core diameter would have been preferred, AX was chosen as the rock samples obtained were relatively small and it was desirable to have more testable samples for each type of test. Cores were first considered for UCS testing if they had any intact sections longer than 60.2mm, giving them the preferred Length/Diameter ratio of 2.

Rocks were cored using a modified radial arm drill with a water cooled bit. After coring, samples were cut using a tile saw in the lengths appropriate for the desired tests. Samples for UCS testing were cut to a length of approximately 2.5”. Since core diameter was roughly 1.24”, a length of 2.5” allowed for some length to be removed when grinding the ends of the cylinders.

After cutting, the ends of specimens for compressive testing were polished flat and parallel using a rotary surface grinder. The grinder (Figure 30) rotates the specimen while the grinding wheel oscillates back and forth. Once the specimen makes contact

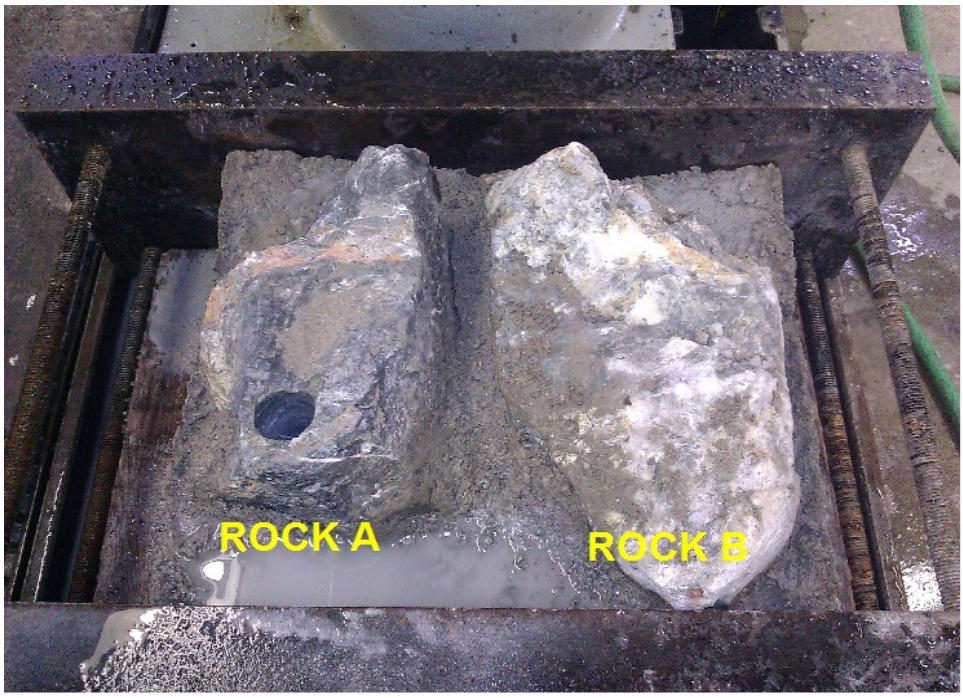

Figure 29: Rocks from Beck St. Quarry, cast in concrete and clamped in place, ready for drilling

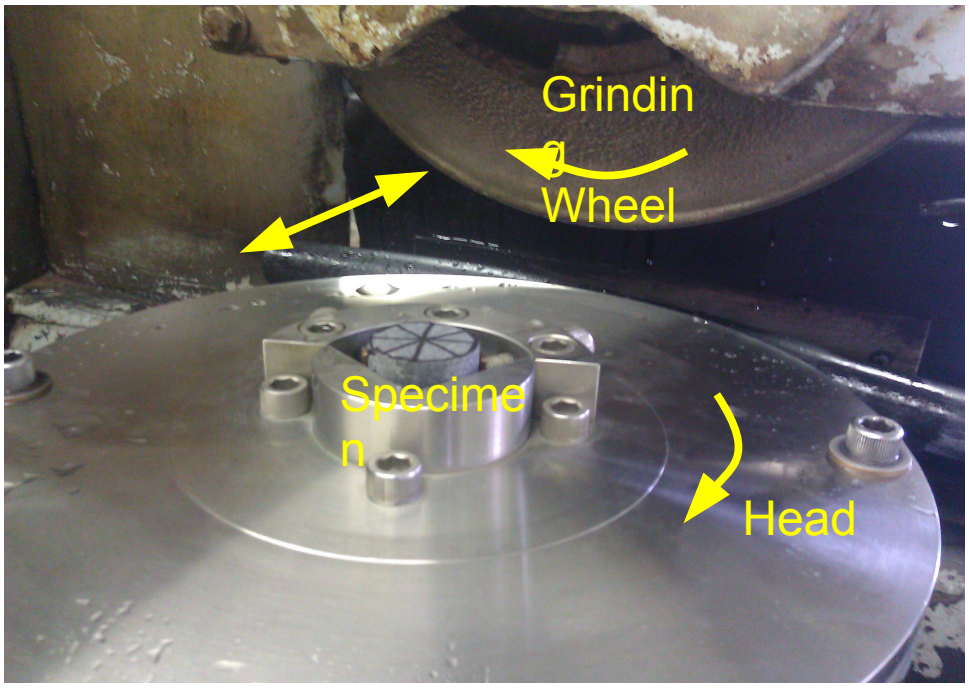

Figure 30: Grinding Setup

with the grinding wheel, it is ground in 0.001” increments until the surface is flat. As a guide, lines were drawn across the end of the specimen with marker. Once the lines were all ground off, it was supposed that the original surface of the rock was completely gone and thus had been ground to a uniform surface. After grinding, the head was flipped over, re-secured, and the grinding process was repeated for the other end of the cylinder.

After grinding, samples were checked for end parallelism using a micrometer (Figure 31). Cylinder ends on all specimens were determined to be parallel to within a tolerance of 0.002”.

After preparing samples for UCS testing, any leftover pieces of core longer than 15.05mm were prepared for use as discs in the Brazil test. Discs were only cut, not polished, and dimensions measured using a micrometer accurate to 0.01mm.

Each rock was individually labeled according to the rock and hole it came from. For a segment of core to be usable for UCS testing, it had to have a L/D ratio of approximately 2. For shorter cores, a short core correction was used. Tables 2-4 list the number of samples obtained from each rock.

4.4.2 Description of Rock Testing Machine

A small testing frame custom made for testing AX core was used in the University of Utah's rock lab. The frame can accept two hydraulic cylinders for loading: one capable of a 20,000 lb load and one capable of a 60,000 lb load. These cylinders can be changed depending on the strength of rock. Similarly, three different load cells can be used- one with a capacity of 2500 lb, one with a capacity of 10,000 lb, and one with a capacity of 50,000 lb. Again, the choice of load cell is dependent on the strength of rock and the test being performed. The lower the capacity of the load cell, the finer the sensitivity, hence

Figure 31: Testing compressive sample for end parallelism

Table 2: Samples obtained from limestone at Beck St. Quarry

Rock	Holes Drilled	UCS specimens	Brazilian Discs
A	5	2	4
B	8	5	5
C	6	6	8
D	3	0	0

Table 3: Samples obtained from limestone at gypsum mine

Rock	Holes Drilled	UCS specimens	Brazilian Discs
A	8	8	9
B	9	8	12

Table 4: Samples obtained from gypsum

Rock	Holes Drilled	UCS specimens	Brazilian Discs
E	8	6	10
F	5	6	10

the smallest load cell possible should be used.

To measure elastic modulus, an axial displacement meter (DCDT) is attached through the center of the hydraulic cylinder, which has a hollow ram (Figure 32). This allows displacement to be measured axially, rather than by averaging the results from two side-mounted sensors.

For compressive testing, data are recorded using a two-channel Nicolet 310 storage oscilloscope. The oscilloscope can store up to 40,000 data points for export to a spreadsheet program. Time interval for data recording can be set manually. Two Omega Model DP25B-S-A panel meters are connected to the oscilloscope- one output displacement from the DCDT and one output force on the load cell. The panel meters (Figure 33) output a voltage to the oscilloscope. Voltage is converted to stress and strain

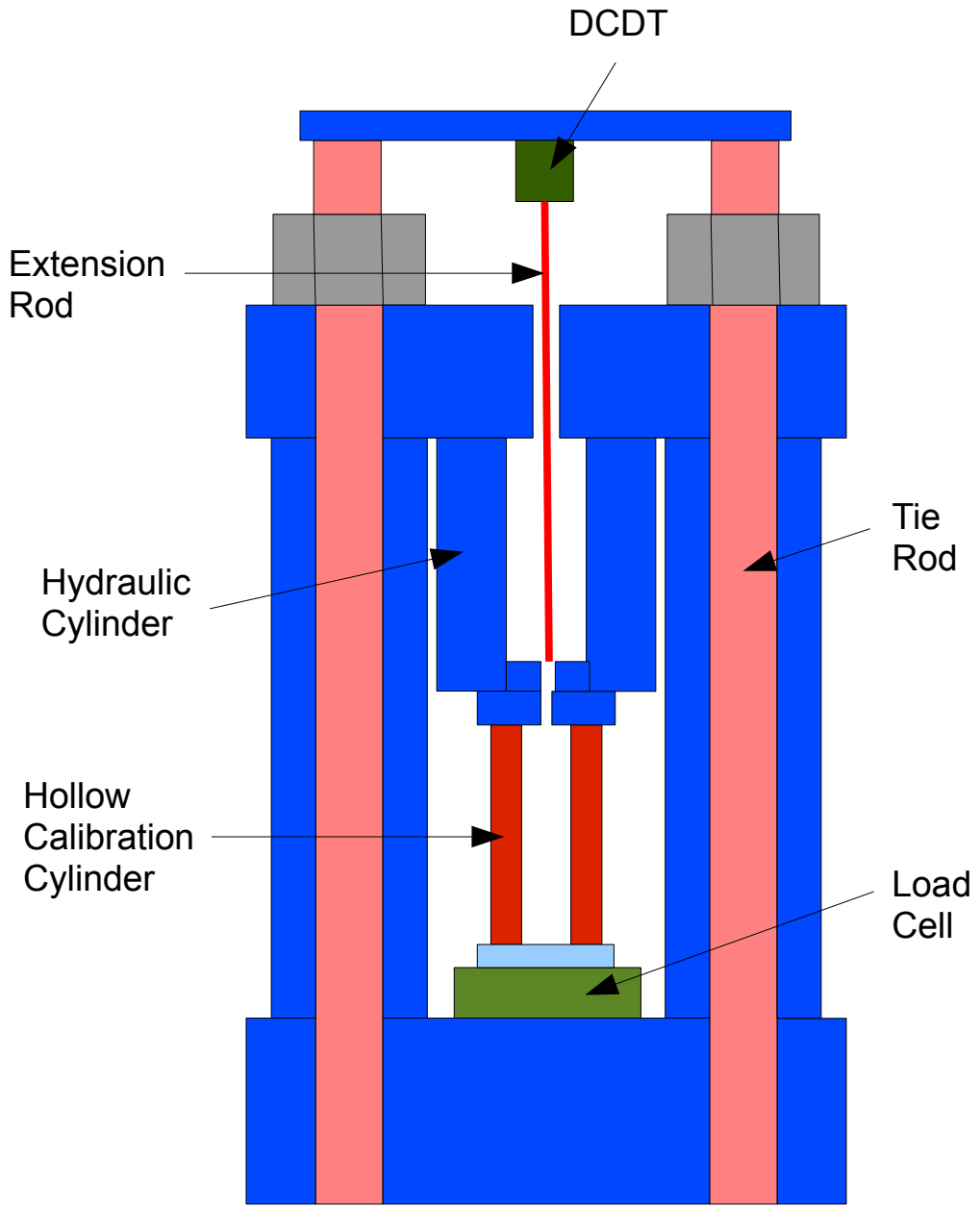

Figure 32: Schematic of test frame. After McCarter (2009)

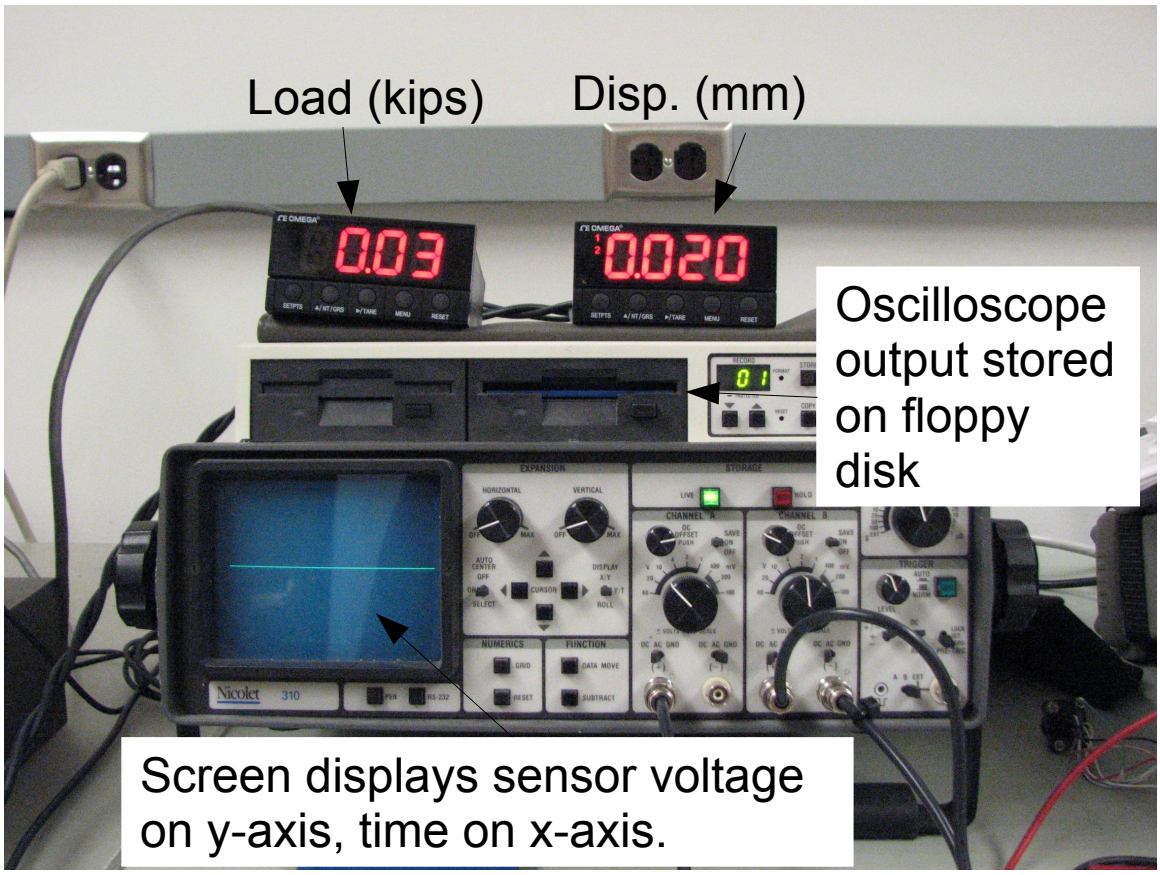

Figure 33: Data recording system on rock testing frame

in postprocessing.

For tensile testing, no oscilloscope is necessary as the Omega Model DP25B-S-A meter can record the maximum value of force on the load cell and displacement is not needed.

4.4.3 Testing of Rock Samples

Samples from all three blasts were tested for the following parameters:

- Tensile strength
- Compressive Strength
- Elastic Modulus

Tensile testing using the Brazil test was accomplished using the 2500 lb load cell, which had sufficient capacity to test all but one of the tensile samples, which came from the limestone at the gypsum mine. Specimens were placed between circular platens. Loading was accomplished through a hand pump. So although a true constant strain rate was not possible, pumping was done at a slow rate with the intention of causing breakage in about two minutes. The oscilloscope was set to record force and displacement at 50 ms intervals and had the capacity to record up to 4,000 points, allowing 200 seconds of recording.

Unconfined compressive strength testing was performed using the 50,000 lb load cell, and this load cell was sufficient for all compressive testing. Specimens were placed between a spacer and a spherical seat in order to eliminate edge loading on the specimens. Loading was accomplished through a hand pump. So although a true constant strain rate was not possible, pumping was done at a slow rate with the intention of causing breakage in about two minutes.

4.5 Data Processing

4.5.1 Photogrammetry

Photogrammetric analysis was completed using two programs from ADAM Technology: 3DM CalibCam and 3DM analyst. 3DM CalibCam was used to mosaic photos and correct lens distortion from the images, and 3DM Analyst was used to create 3D models of the rock faces.

In 3DM Calibcam, the correct camera calibration file was chosen. This was an important step as it would correct lens distortion later in the process. Then, stations corresponding to the camera stations employed in the field were created. Each image was

assigned to the camera station at which it was taken (Figure 34). A mosaic was produced from each station using 3DM CalibCam's "create merged image" option. Merged images are automatically corrected for lens distortion and come out "photogrametrically correct." (ADAM 2010)

In 3DM analyst, pairs of mosaics were used. First, control points were entered. Next, a bundle adjustment was performed to assure low residuals in the final project. Precision was not of great concern, but residuals under 10cm were preferred. 3D models were produced (Figures 35, 36). Models produced in 3DM could then be manipulated in 3D space.

4.5.2 Joint and Bridge Delineation

Once photogrammetry was used for scale, 2D images were processed to delineate joints and bridges, as well as determine in-situ block size. Image processing, from uploading photos to the final product, generally took about 5 hours for each imaged highwall. The same stitched panorama images used in 3DM analyst were also used for image processing in order to be consistent in data input. Furthermore, 3DM CalibCam corrects images for lens distortion, which leads to more accurate images.

Joint and rock bridge delineation was performed using Split Engineering's Split FX software package. Split FX is rockmass characterization software that has the ability to manually delineate traces. Automated software package WipFrag was considered for the task, as it purports to automatically detect joints in rock faces. However, hours of attempts with all highwall images failed to produce acceptable results, even after numerous adjustments to detection parameters. Therefore, the much slower but ultimately better procedure of manual delineation was chosen.

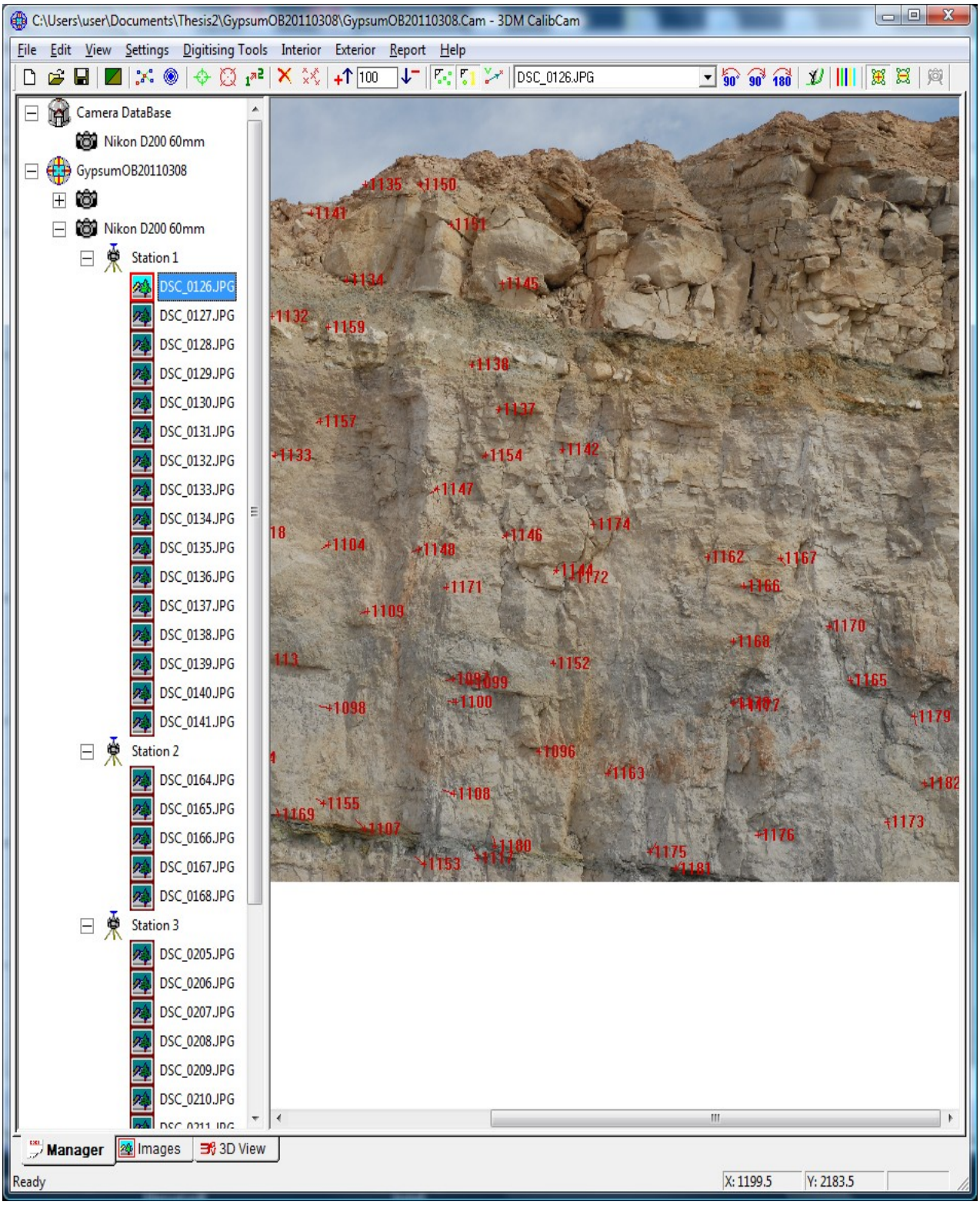

Figure 34: Screenshot showing camera stations and images before mosaicking

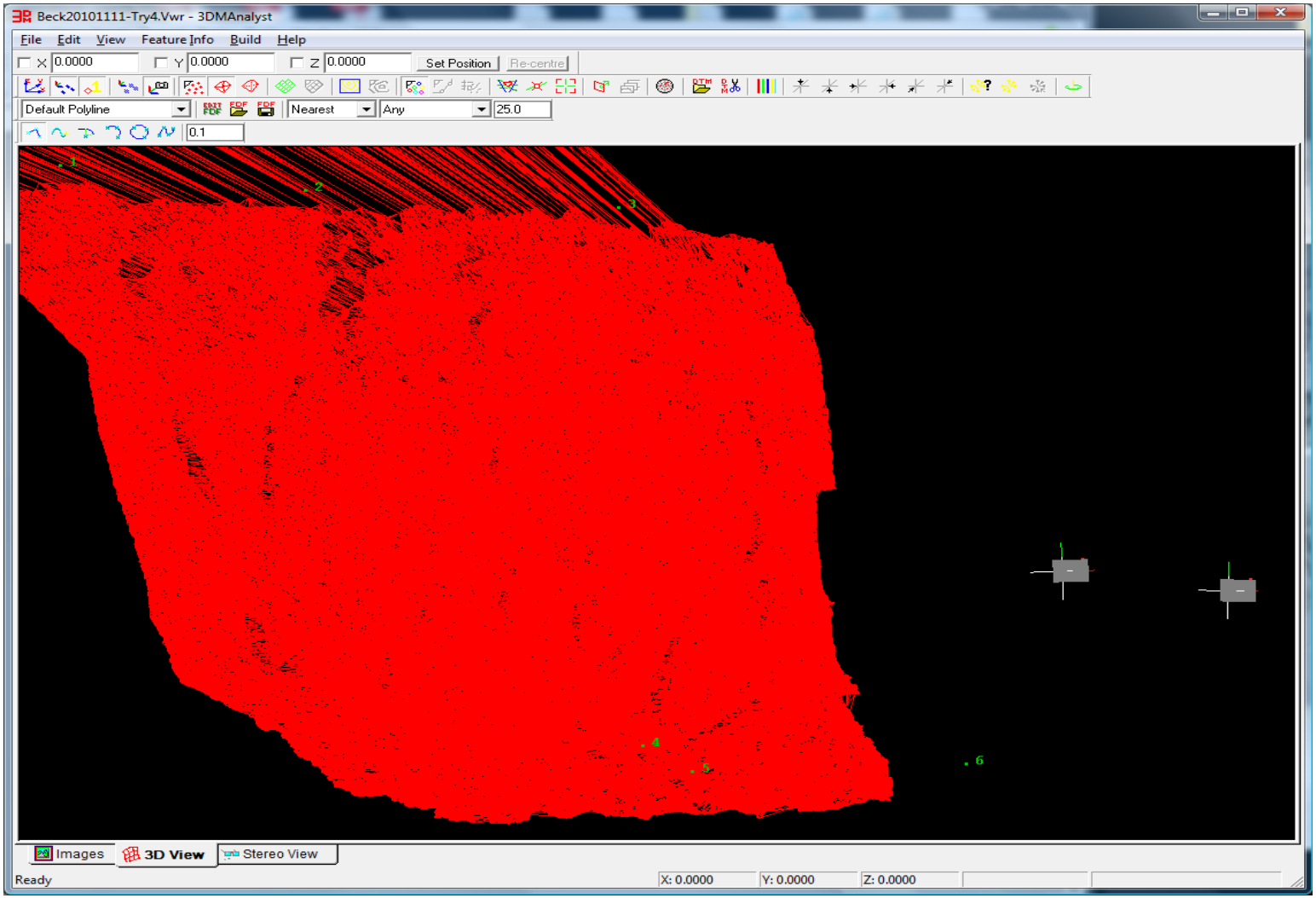

Figure 35: Screenshot showing 3D point cloud of rock face

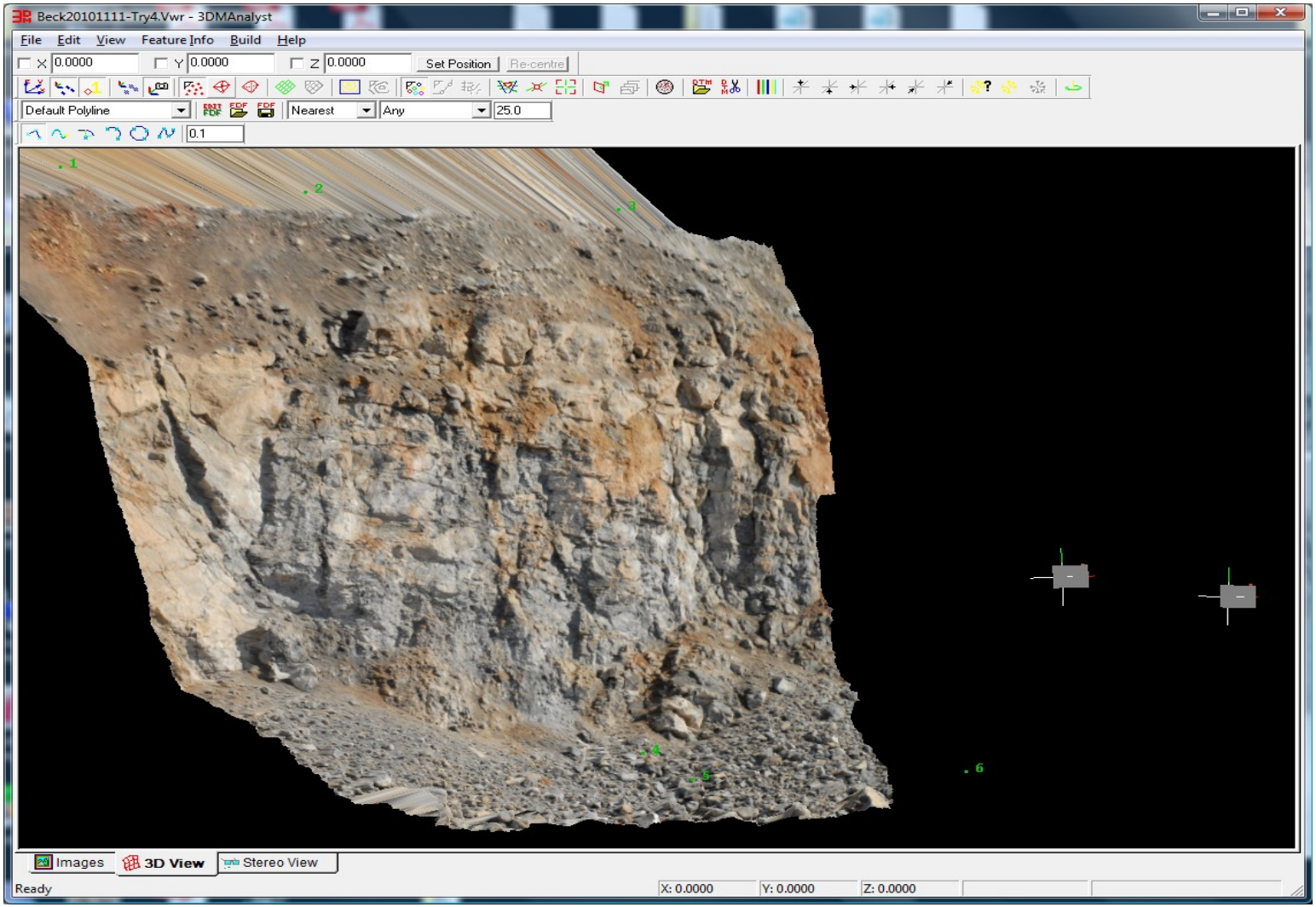

Figure 36: View of the same rock face, with image draped over

Procedure for delineating traces in Split FX is relatively straightforward. The user must first add the desired image to the file. However, the maximum image size usable in Split FX is around 1300x900 pixels. Therefore, it was necessary to crop the images to the proper size. Another possibility would have been to resize the image, but this would have led to an unacceptable reduction in ground pixel size and a subsequently diminished capacity to detect small features. Images were cropped to regions which appeared representative of the whole highwall.

The cropped image was then imported into Split FX. First, joints were delineated manually using the Split FX trace delineation tool. The tool allows the user to draw polylines on the rock face, and stores data on the properties of the lines. The finished product is shown in Figure 37.

After delineating existing joints, rock bridges had to be filled in. Rock bridges needed to be segregated somehow from joints, and Split FX only allows one set of traces on an image. Therefore, the image with joints delineated was exported, and then added to the project in Split FX. Then, rock bridges were delineated in a different color. Although the delineation of rock bridges is somewhat subjective, two rules were followed:

1. Rock bridges will extend existing joints in a straight line
2. A rock bridge ends when it intersects either an existing joint, another rock bridge, or the edge of the photo.

As shown in Figure 38, the combination of rock bridges and joints suggests 2D in-situ rock blocks. In order to make these blocks readily processed by edge detection software, several steps were undertaken. First, the final image (for example, that shown in Figure 32) was exported as a .bmp file and opened in GIMP, a free open-source image editing software package. Using GIMP's color selection tool, all pixels the color of the

delineated traces (both joints and bridges) were selected and pasted into a new layer. The original layer containing an image of the rock face was deleted, leaving an image that showed outlines of in-situ blocks.

An image containing only traces (Figure 39) was fed in to WipJoint, a computer program that is designed for edge detection and analysis of in-situ rock blocks. Although it was noted previously that WipJoint did not work satisfactorily with an image of the rock face, when presented with black lines on a white background it performed admirably.

Once the image was scaled in WipJoint, it detected blocks automatically and returned a statistical analysis of block size.

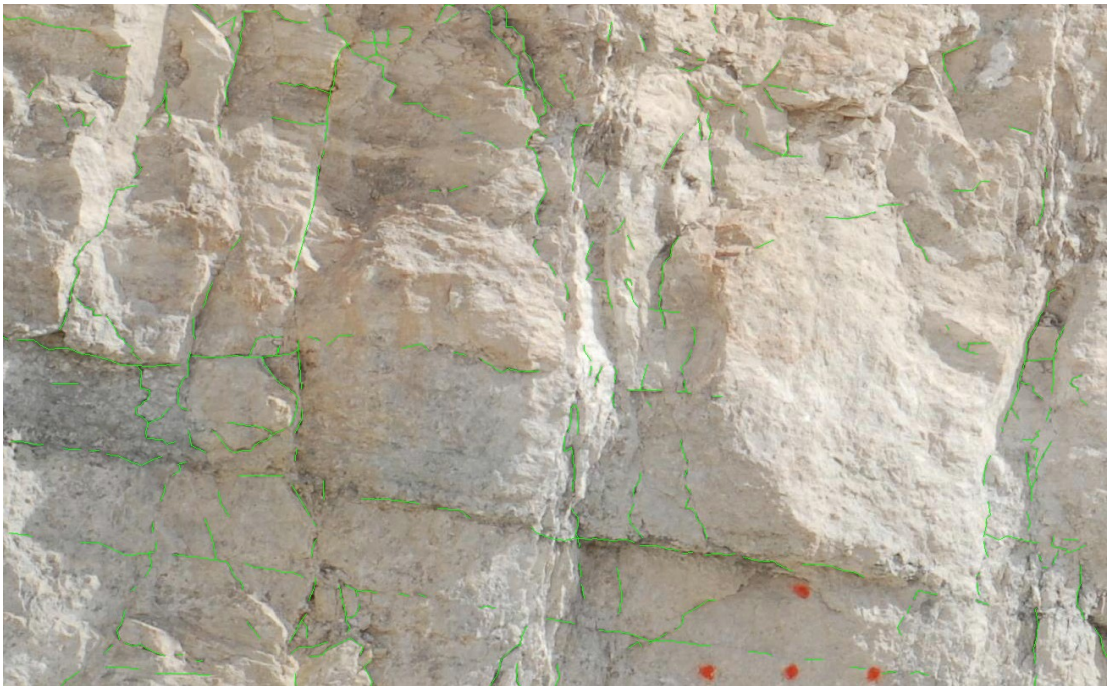

Figure 37: Manual delineation of existing rock joints

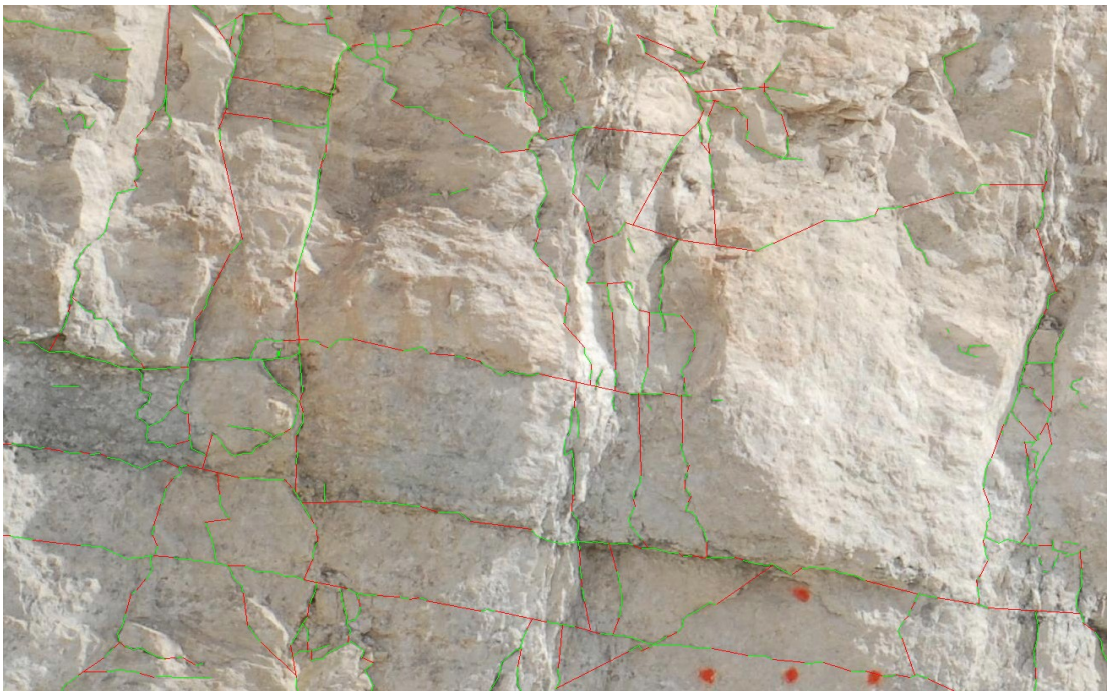

Figure 38: Rock bridges outlined on top of image with joints

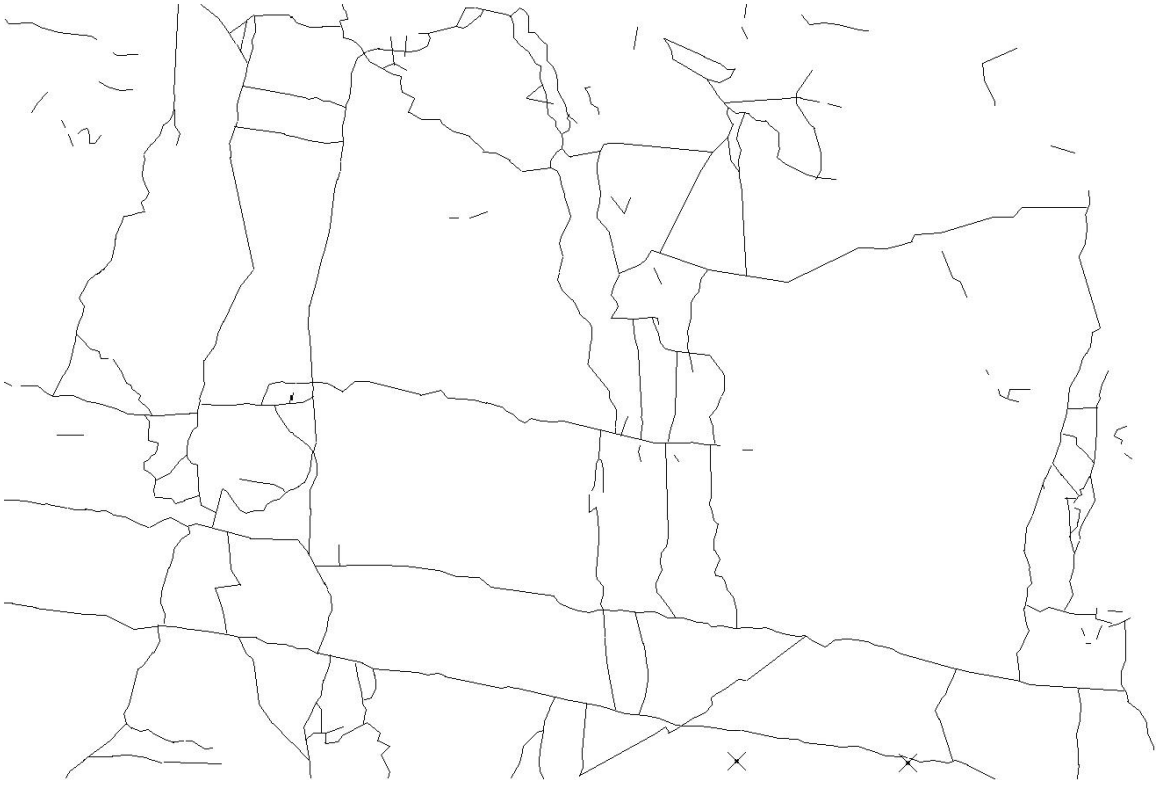

Figure 39: Outlines of in-situ blocks, no rock showing

CHAPTER 5

RESULTS

Chapter 6 contains a summary of all results from rock strength testing to evaluation of blasting fragmentation. Raw data of all results can be found in appendices. Appendix A contains full results of rock strength testing for all samples. Appendix B contains all data relevant to analysis of in-situ block size, and Appendix C contains all data relevant to muckpile particle size analysis. Appendix D show joint orientation data on stereonets which were used for determining rock factor in the Kuz-Ram model.

5.1 Strength of Intact Rock

Rock strength properties, necessary for employment of the Kuz-Ram model, are summarized in the following tables. The strongest rock was the limestone overburden, and the weakest rock was the gypsum. Both limestones failed rather energetically in compression; samples tended to break suddenly in to many small fragments. The gypsum often had a significant amount of plastic deformation (Figure 40) before fracturing and brittle failure became apparent (Figure 41).

Tensile testing using the Brazilian test was successful, with diametric cracks causing failure in all specimens. As with compressive testing, the limestone overburden from the gypsum mine was strongest, and gypsum was the weakest. Figure 42

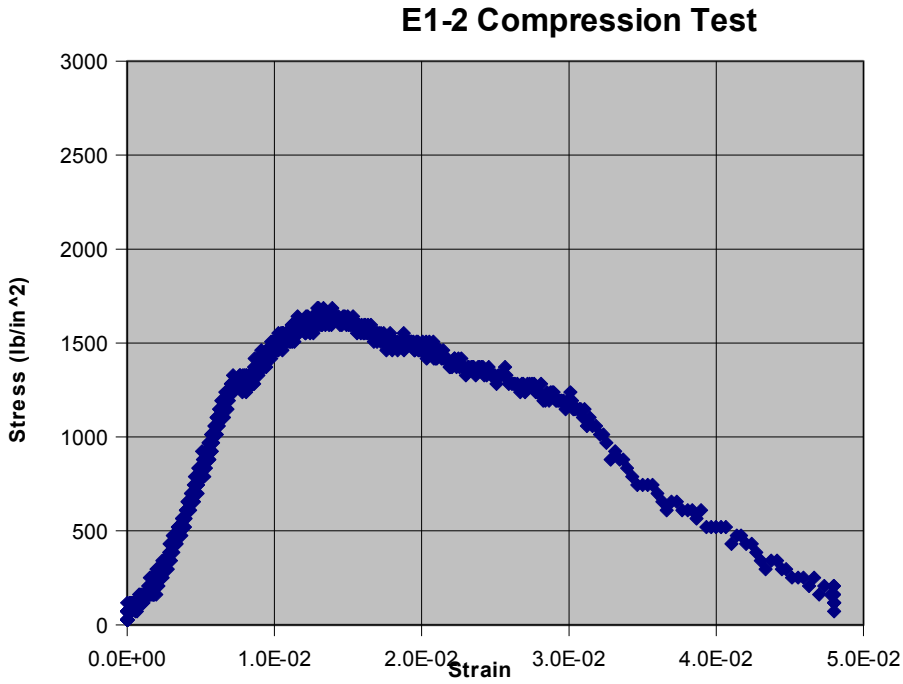

Figure 40: Stress-strain curve showing plastic deformatioin in a gypsum specimen

Figure 41: Highly broken limestone (left) and more cleanly failed gypsum (right)

summarizes the mean compressive and tensile strength, elastic modulus, and density of the three rock types. Fully detailed results, including stress-strain curves, can be found in Appendix A.

Although both limestones produced tightly distributed results, the gypsum showed a bimodal distribution of strength. Cores of gypsum were drilled from two rocks, labeled E and F. Samples from rock E were considerably weaker in tension and compression than samples from rock F. Samples from rock E had a mean compressive strength of 11.3 MPa while samples from rock F had a mean compressive strength of 25.6 MPa. Likewise, the tensile strength of rock F was roughly twice that of rock E: 4.4 MPa and 2.2 MPa, respectively.

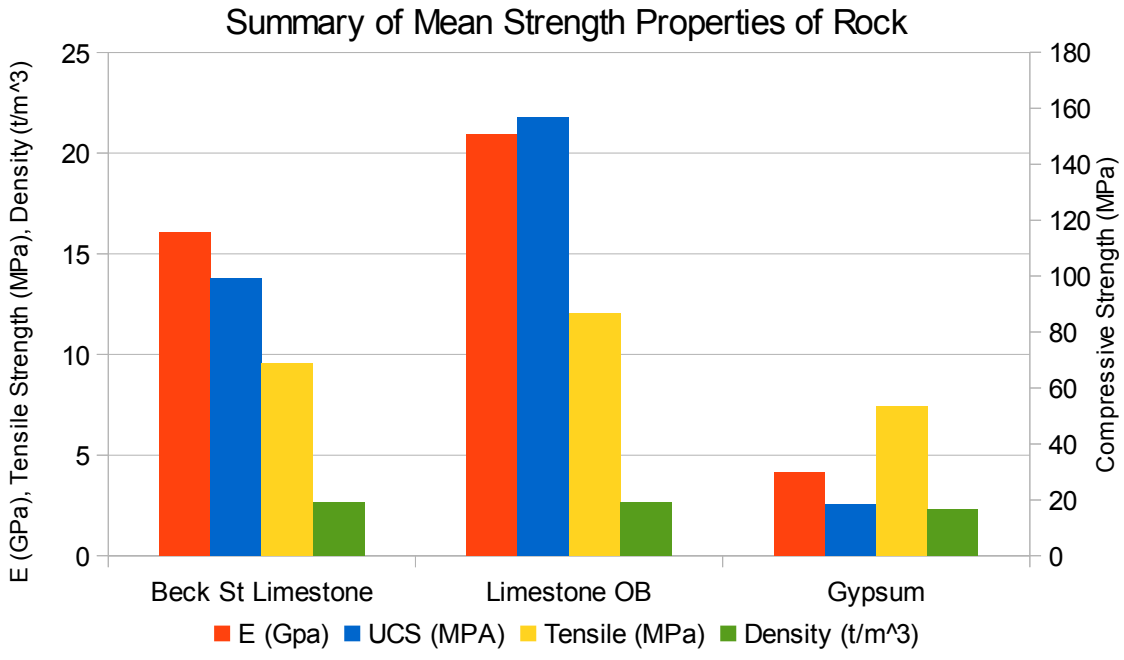

Figure 42: Rock strength properties

5.2 Rockmass Characterization

Rockmass characterization was performed on 3D rock face models. The step was necessary in order to characterize joint properties for use with the Kuz-Ram model. The following tables summarize the predominant joint sets. Stereonets are included in Appendix D.

Based on the orientations given in Table 5, the limestone is predominated by vertical jointing. It shows a bedding plane does not dip steeply and strikes nearly perpendicular to the face. The rock was therefore assigned a JPA of 30. Spacing of the vertical joints was between 0.1m and Oversize and therefore assigned a JPS of 20. Since rock was neither powdery nor massive but vertically jointed, RMD was the sum of JPS and JPA, equal to 50.

Gypsum (Table 6) has one vertical joint set and one set that dips out of the highwall, giving it a JPA of 20. Vertical joint spacing was over 0.1 m and therefore assigned a JPS of 20. Since rock was neither powdery nor massive, RMD was the sum of JPS and JPA, equal to 40.

The limestone overburden (Table 7) has a bedding plane that dips in to the highwall, giving it a JPA of 40. JPS was assigned a score of 50 for vertical joint spacing on the scale of the drilling pattern. RMD was assigned a score of 50 for massive rock.

Table 5: Joint sets in Beck St. Quarry limestone

	Dip	Dip Direction
Highwall	77.1	243.9
Joint set 1	80.7	209.6
Joint set 2	85.1	85.3
Bedding Planes	18.6	140.1

Table 6: Joint sets in gypsum

	Dip	Dip Direction
Highwall	51.5	170.1
Joint set 1	19.1	227.0
Joint set 2	84.9	221.5

Table 7: Joint sets in limestone overburden

	Dip	Dip Direction
Highwall	82.1	165.2
Joint set 1	83.9	197.3
Joint set 2	89.0	128.1
Bedding Planes	10.5	43.7

5.3 Properties of Traces

Properties of rock bridges varied significantly between rocks. Joint persistence varied from a low of 64% in the limestone overburden at the gypsum mine to a high of 84% in the gypsum. Distribution of lengths of traces is shown in Figures 43-45.

The distribution of trace lengths in the Beck St. Quarry (Figure 43) case shows positive skew. Both traces and bridges have a median length lower than the mean. The average bridge length was about half the joint length (Table 8).

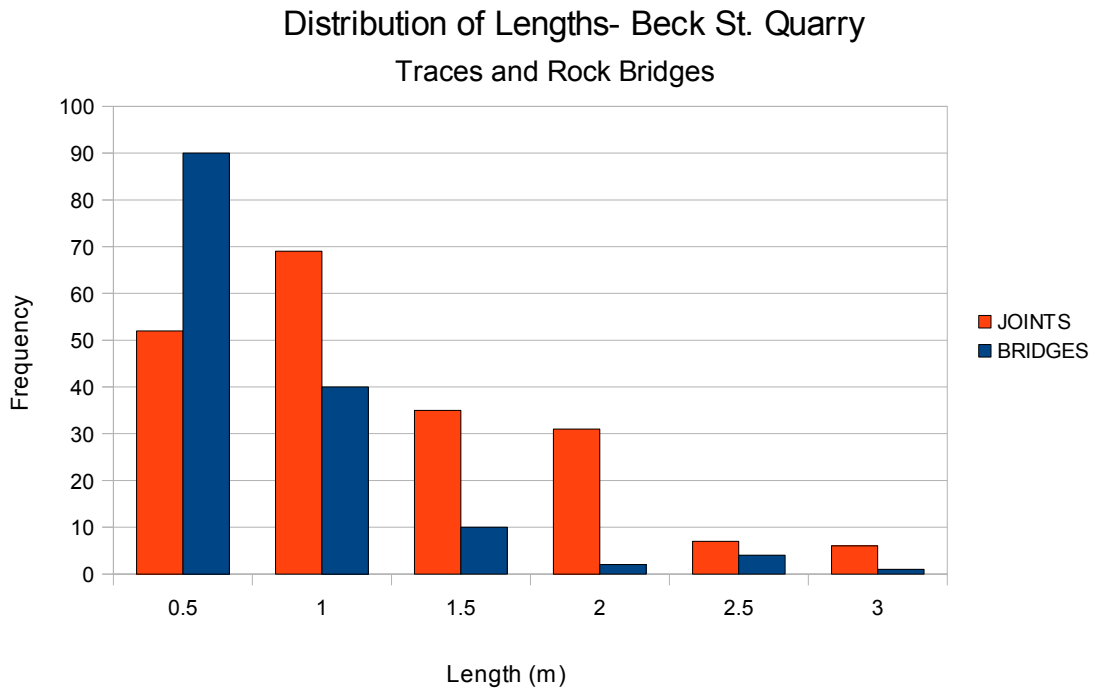

Figure 43: Histogram showing lengths of traces on Beck St. quarry highwall

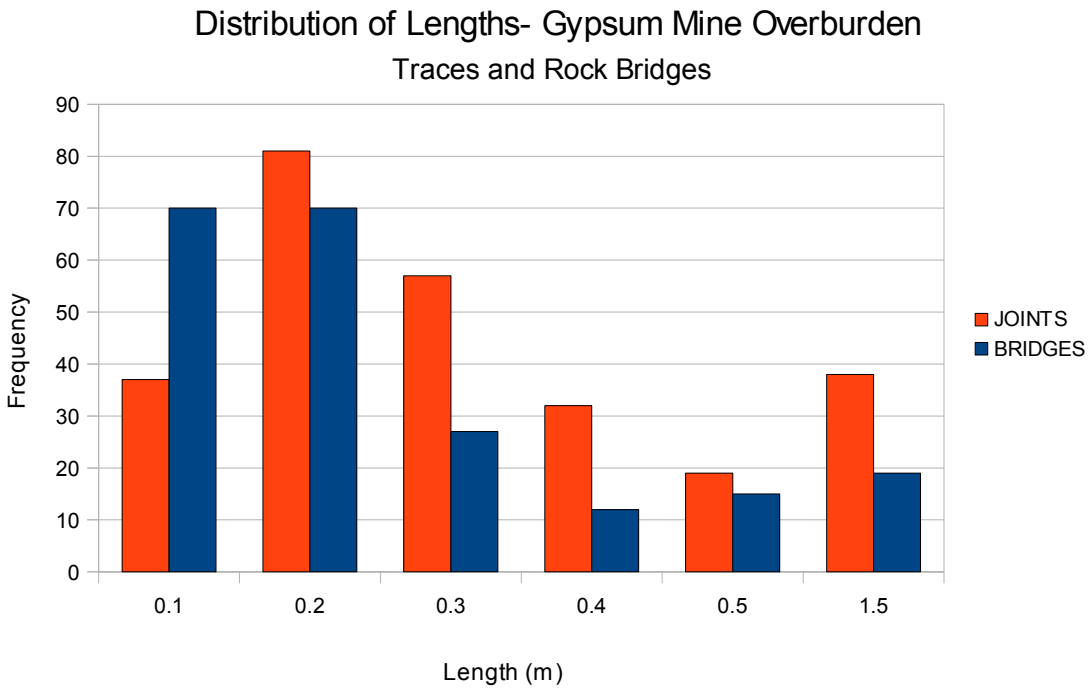

Figure 44: Histogram of trace lengths on limestone overburden highwall

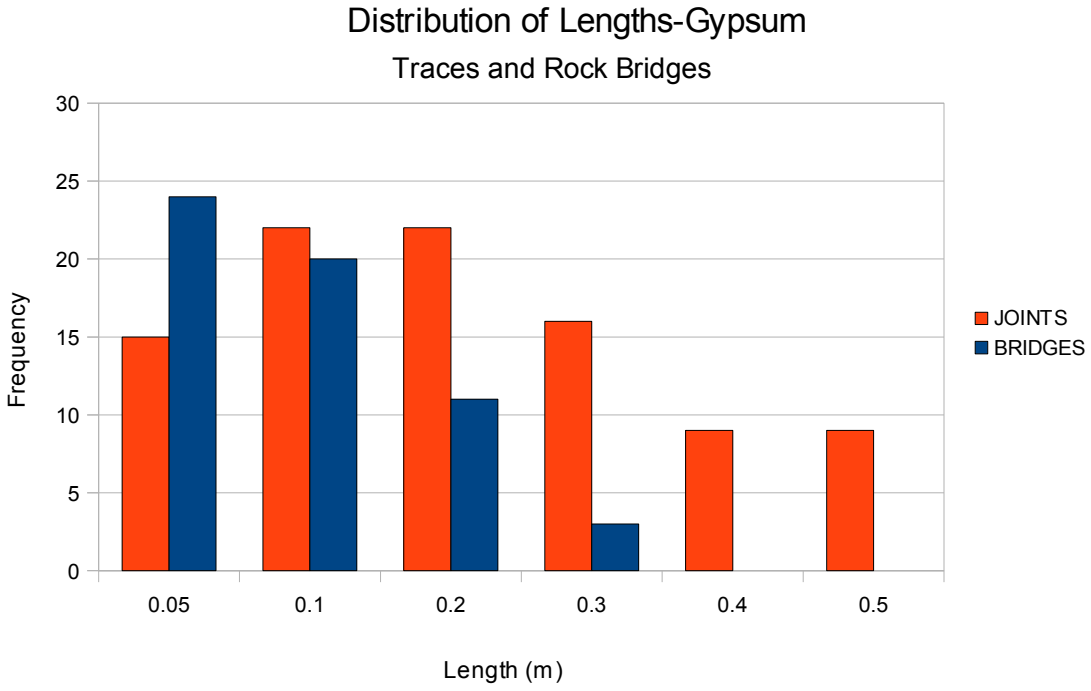

Figure 45: Histogram of the lengths of joints and bridges in the gypsum

Table 8: Statistical summary of trace lengths-Beck St. Quarry

	JOINTS	BRIDGES
Min	0.11	0.09
Max	5.38	2.83
Std. Dev	0.84	0.47
Mean	1.08	0.57
Median	0.87	0.43

Figure 44 shows that again, the distribution is positive skewed so that in both cases median length is lower than mean length. As with the Beck Street limestone, joints tended to be longer than bridges. However, the difference in mean length is not as pronounced as it was in the Beck Street limestone; the mean length of a joint is only about 1.5 times the length of a trace (Table 9).

In the gypsum (Figure 45), distribution of bridge lengths was not as skewed, with a skewness of 1.39 compared to a skewness of 3.1 for joints. The average joint was about three times the length of the average bridge (Table 10).

Interestingly, the project discovered a remarkably consistent correlation between the number of joints and the number of bridges in each highwall surveyed. The finding can be summarized by

$$B = 0.93\mathrm{J} - 37.21 \tag{6.1}$$

where B is the number of bridges on the highwall and J is the number of joints (Figure 46).

Table 9: Statistical summary of trace lengths-limestone overburden

	TRACES	BRIDGES
Min	0.03	0.02
Max	1.56	1.01
Std. Dev	0.25	0.19
Mean	0.30	0.21
Median	0.23	0.14

Table 10: Statistical summary of trace lengths-gypsum

	JOINTS	BRIDGES
Min	0.01	0.01
Max	1.78	0.27
Std. Dev	0.26	0.06
Mean	0.23	0.08
Median	0.17	0.06

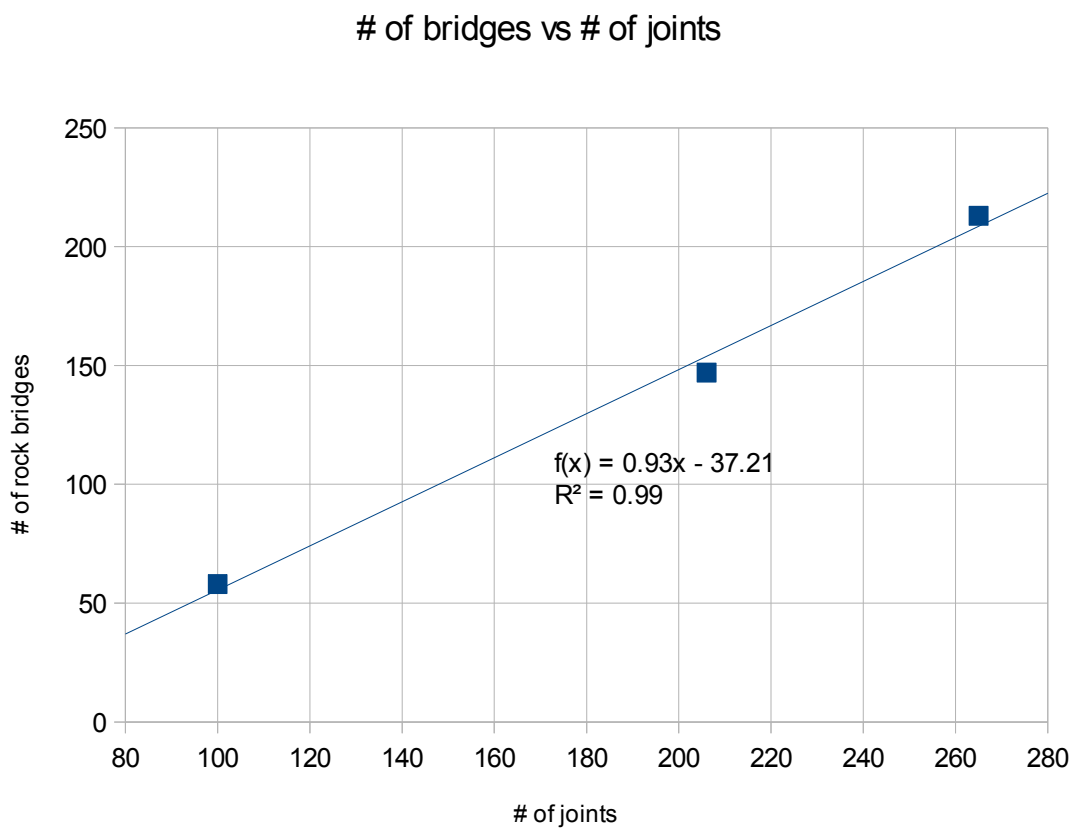

Figure 46: Strong correlation between number of joints and number of bridges at all three sites

5.4 The Effect of Rock Bridges on Comminution Factor

To determine the effect of rock bridges on the comminution factor, various properties of the bridges were compared to the comminution factor at each site. First, the ratio of bridge length to joint length, dubbed the bridge-joint length ratio was considered. The bridge-joint length ratio was defined as:

$$\Omega = \frac{\sum_{i=1}^{m} L_m}{\sum_{i=1}^{n} L_n} \tag{6.2}$$

where

m= number of bridges on a given highwall

L_m = length of bridge *m*

n= number of joints on a given highwall

L_n = length of joint *n*.

The effect of bridge-joint length ratio and other properties of the intact rockmass were examined for any possible correlation with comminution factor. Figure 47 shows that a higher value of Ω leads to a smaller comminution factor, i.e., longer bridges lead to more intense fracturing of the rock mass.

Figure 48 shows comminution factor as a function of trace density. Neither the number of joints nor the number of traces per unit area seems to have any correlation with comminution factor.

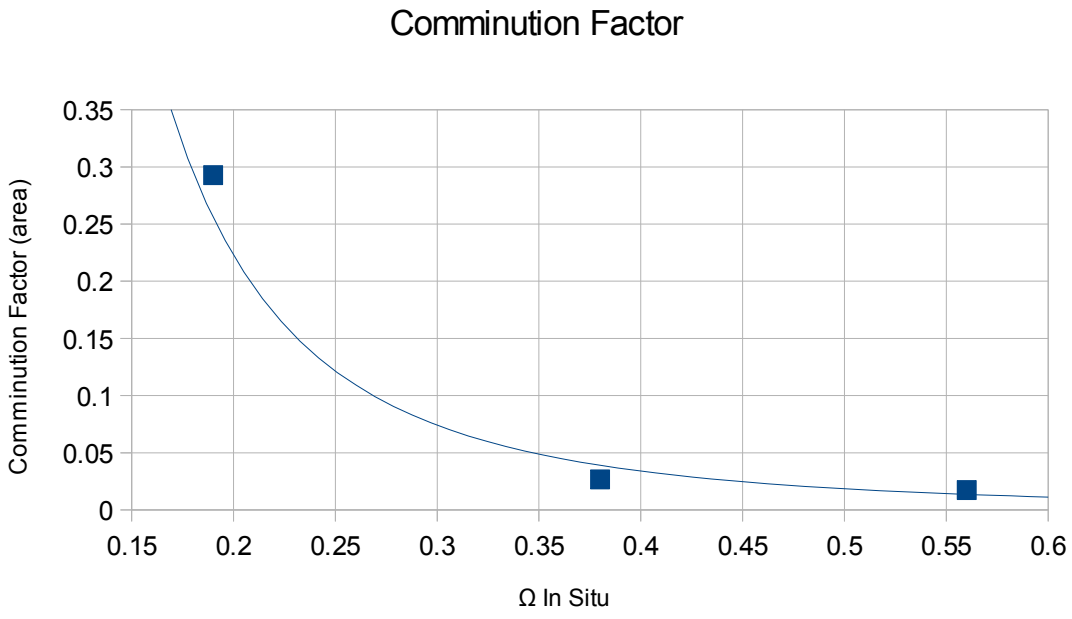

Figure 47: Comminution Factor as a function of Ω

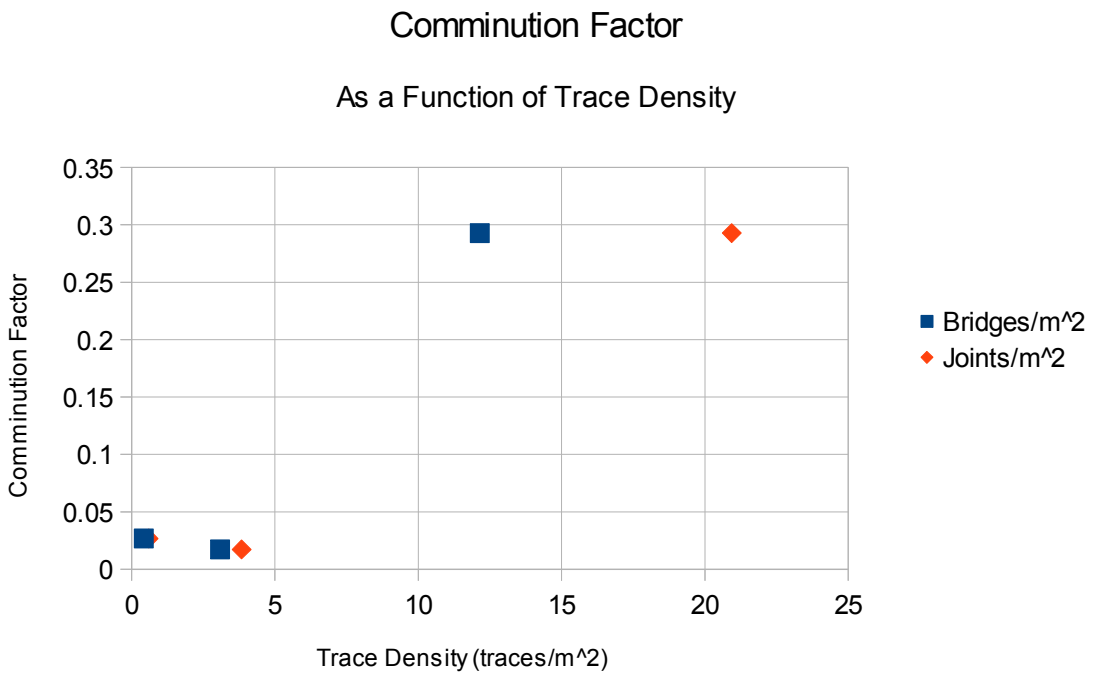

Figure 48: No apparent correlation between trace density and comminution factor

5.5 Comparison to Empirical Model

When compared to fragmentation predicted by the Kuz-Ram model, there is, invariably, some variation between prediction and reality. Fragment size distribution predicted by the Kuz-Ram model was compared to the actual fragment size distribution as measured by Split Desktop.

Figure 49 shows a comparison of sieve analysis curves from the limestone at the Beck Street quarry. Visual inspection reveals a few obvious differences between expected and actual fragmentation. The Kuz-Ram model predicted more fines, and indeed a smaller overall particle size. Kuz-Ram predicts a median particle size of 21.4 cm, while in actuality median particle size was 31 cm. The Kuz-Ram prediction deviates from actual results by -31%.

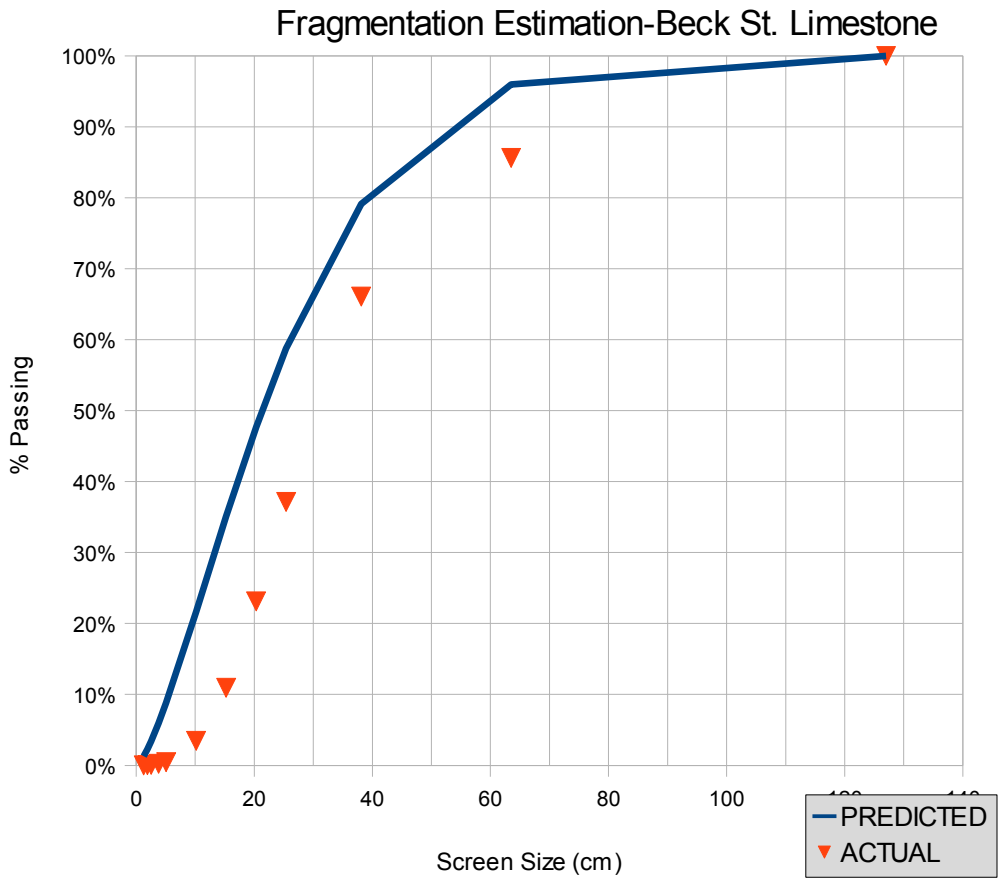

Figure 49: Fragmentation- Kuz-Ram prediction compared to actual

Figure 50 shows a comparison of sieve analysis curves from the limestone overburden at the gypsum mine. Of the three blasts, the Kuz-Ram model predicted this one best. The Kuz-Ram model predicted a median particle size only 26% below the actual result, 30.7 cm rather than the actual result of 41.4 cm. Unlike the other two blasts, the Kuz-Ram model predicted some values above and some below actual fragmentation passing percentages.

Figure 51 shows a comparison of sieve analysis curves from the gypsum blast. Of the three blasts, the Kuz-Ram model predicted this one the worst. The Kuz-Ram model predicted a median particle size fully 69% below the actual result, 8.0 cm rather that the

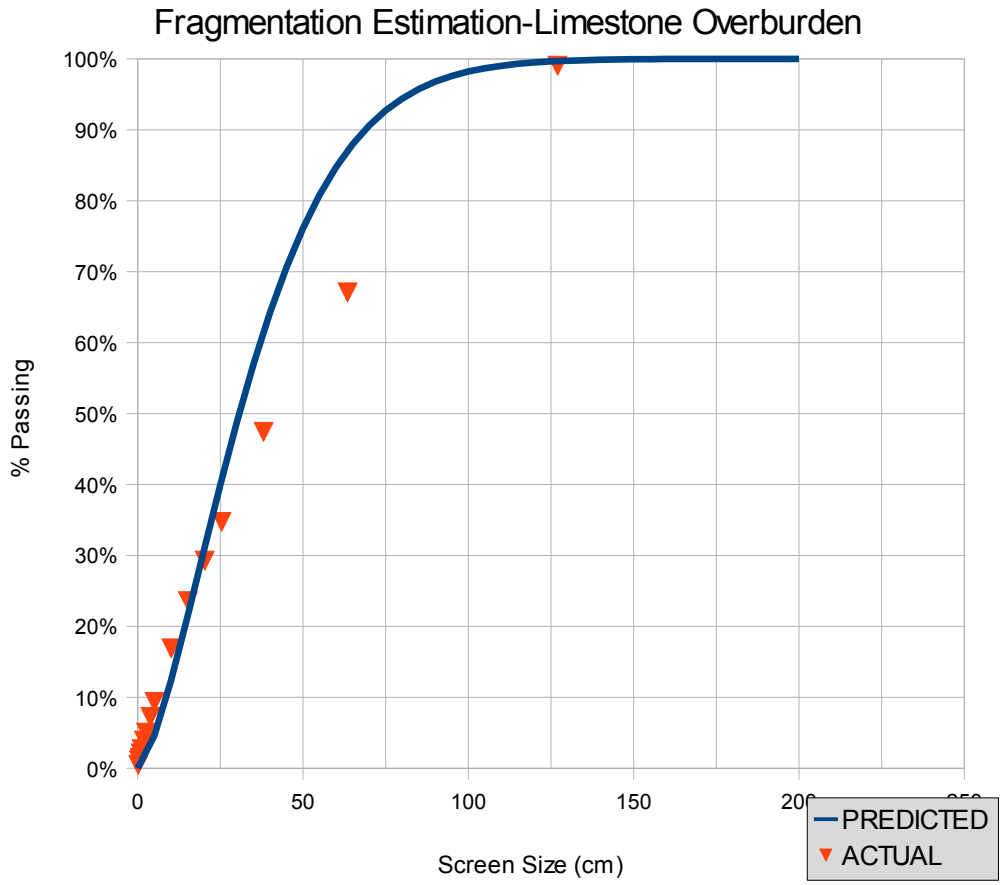

Figure 50 Fragmentation- Kuz-Ram compared to actual

actual result of 5.9.

A summary of the error in Kuz-Ram as a function of Ω is shown in Figure 52. The graph shows a positive correlation between Ω and percent error.

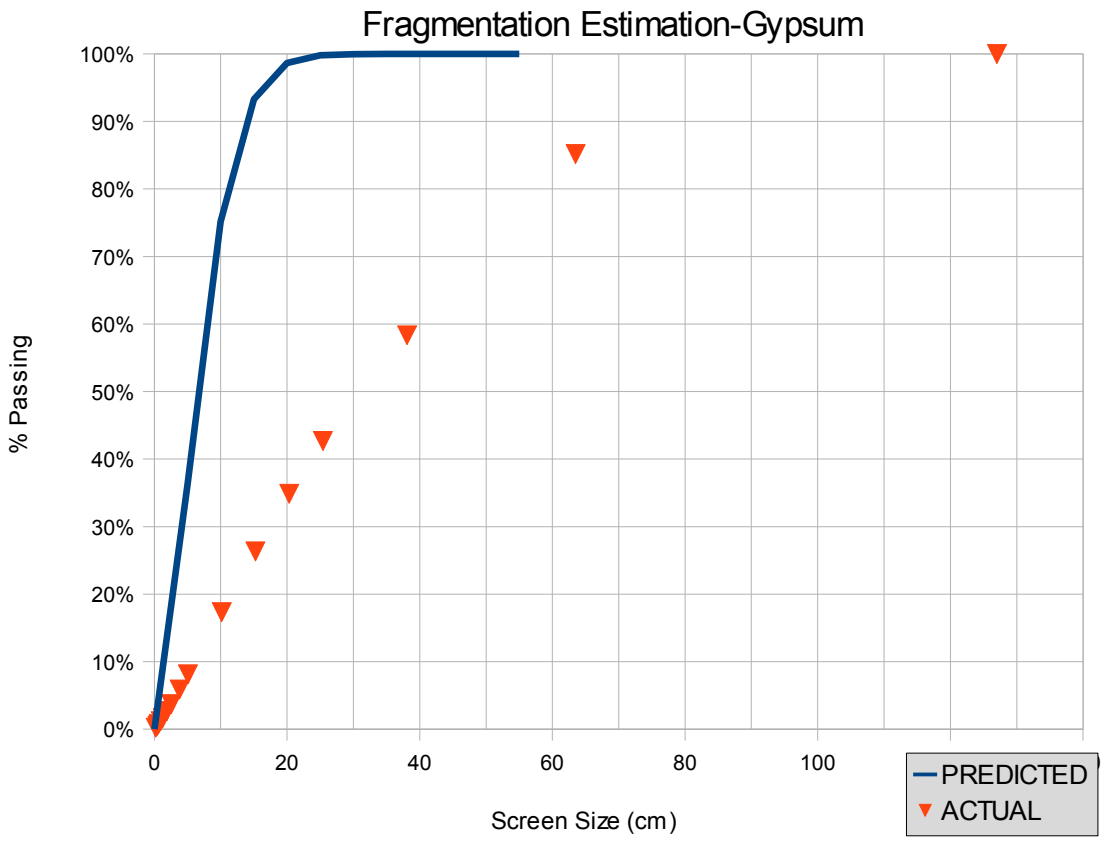

Figure 51: Fragmentation for gypsum blast compared to Kuz-Ram model

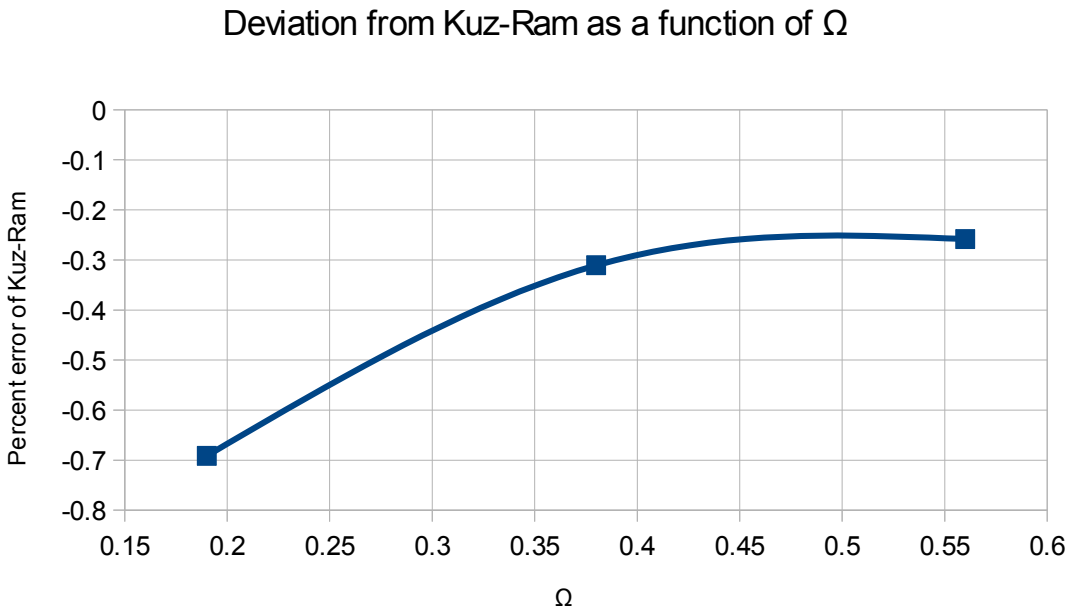

Figure 52: Deviation of actual blasts from Kuz-Ram model, summarized

CHAPTER 6

CONCLUSIONS AND DISCUSSION

Rock bridges in all three rockmasses indeed seemed to have an effect on blasting fragmentation.

For all the ways the data were parsed and analyzed, one correlation stood out consistently when data were analyzed in terms of both comminution factor and when compared to the Kuz-Ram model. In this experiment, a higher value of Ω, the bridge-joint length ratio, was always associated with larger particles after blasting. Rock with a higher value of Ω tended to produce fragments about the same size as predicted by Kuz-Ram, while rock with a lower value of Ω produced fragments much larger than predicted by Kuz-Ram. Similarly, rock with a lower value of Ω was associated with a higher comminution factor, i.e., larger fragments.

Results seem to suggest that fragmentation occurs more readily for an intact rock. While this initially may seem counterintuitive, it makes sense to think that blasting shock waves travel more efficiently through intact rock and lose strength as they cross fractures. Blast energy abates quickly through air, and so it is logical to think that more energy will go in to the rock if it has fewer places to escape.

The bridge-joint length ratio appears to be the only significant factor in determining fragmentation. Lengths of individual bridges and length density of bridges

had no apparent correlation with fragmentation, whether viewed through comminution factor or through the Kuz-Ram model. This suggests that looking at rock bridges alone is insufficient to make generalizations about fragmentation. Rather, bridges must be considered in combination with the joints they interrupt.

Care should be taken in applying these results. All blasts were performed in sedimentary rock, with square blasting patterns and 6.75" boreholes. More research would be needed to determine if these conclusions can apply outside the very specific parameters of this thesis.

Another concern is with the nature of the gypsum. In testing, the limestone broke readily with brittle fracture. However, the gypsum exhibited a significant amount of plastic deformation which can be seen on the stress-strain curves in Appendix A. It is likely that a significant amount of explosive energy went into plastic deformation of the gypsum; the gypsum showed the least fragmentation despite being subjected to the highest powder factor.

There exists much work that could be done to extend the work in this thesis. Although engineers have spent much time creating numerical models of impersistent joints, most of these models have been applied to slope stability. Numerical modeling of blasting is in many respects a nascent field, and there exist many opportunities to model blasts in impersistent joints in an effort to validate the results of this thesis.

Another serious shortcoming in this project was a lack of automation. Currently available commercial software is inadequate to delineate rock joints on a highwall. It would be advantageous to develop better software in order to facilitate automation of the joint delineation process. In this project, it took about 2 hours to delineate joints and bridges on each highwall.

APPENDIX A

RESULTS OF ROCK TESTING

Table 11

Compressive Testing Results from Beck Street Limestones

Sample Name	L (mm)	D (mm)	M (g)	X-sectional Area (mm^2)	Density (kg/m^3)	UCS (psi)	UCS (MPa)	E (ksi)	E (Gpa)
A1α-1	62.28	31.52	129.63	780.30	2667.44	13375.00	92.22	2596.22	17.90
A4α-1	61.23	31.50	127.48	779.31	2671.57	14394.00	99.24	1905.18	13.14
B1α-1	62.17	31.54	127.93	781.29	2633.77	14349.00	98.93	2015.12	13.89
B1α-2	62.26	31.53	127.80	780.80	2628.96	13168.00	90.79	2360.95	16.28
B2β-1	61.72	31.52	127.35	780.30	2644.30	16037.00	110.57	2249.21	15.51
B7-1	59.99	31.55	121.07	781.79	2581.48	10841.00	74.75	2156.29	14.87
B8-1	62.23	31.54	126.16	781.29	2594.83	12384.00	85.38	1635.17	11.27
C1-1	62.16	31.54	131.90	781.29	2715.94	18229.00	125.68	2782.88	19.19
C1-2	62.38	31.54	133.23	781.29	2733.66	16702.00	115.16	2969.30	20.47
C2-1	61.68	31.52	129.55	780.30	2691.73	10358.00	71.42	1899.48	13.10
C3-1	61.91	31.53	131.33	780.80	2716.85	13284.00	91.59	2612.39	18.01
C5-1	61.07	31.53	129.95	780.80	2725.28	16795.00	115.80	2329.21	16.06
C6-1	61.77	31.50	130.40	779.31	2708.88	17075.00	117.73	2819.99	19.44

	Density (kg/m^3)	UCS (psi)	UCS (MPa)	E (ksi)	E (Gpa)
Mean	2670.36	14383.92	99.17	2333.18	16.09
Median	2671.57	14349.00	98.93	2329.21	16.06
Std. Dev	50.45	2456.51	16.94	407.21	2.81
Min	2581.48	10358.00	71.42	1635.17	11.27
Max	2733.66	18229.00	125.68	2969.30	20.47

Table 12

Tensile Testing Results from Beck Street Limestone

Sample Name	Length (mm)	Diameter (mm)	Mass (g)	Force (lb)	Strength (psi)	Strength (MPa)
A1-A	16.97	31.51	33.83	1215	933.24	6.43
A1-2	16.88	31.5	33.42	1341	1035.84	7.14
A3-1	16.48	31.53	34.15	1435	1134.27	7.82
A3-2	16.83	31.54	34.46	1769	1368.76	9.44
B2-1	16.71	31.49	33.78	1764	1376.88	9.49
B3-1	16.05	31.54	33.39	1729	1402.83	9.67
B3-2	16.6	31.53	33.71	1373	1077.42	7.43
B4-1	16.94	31.5	35.64	2208	1699.50	11.72
B6-1	16.13	31.57	33.75	1882	1517.95	10.47
C2-1	16.81	31.55	35.46	1819	1408.68	9.71
C2-2	16.65	31.54	35.61	1782	1393.73	9.61
C2-3	16.37	31.55	34.78	2045	1626.27	11.21
C3-1	17.03	31.54	35.23	1883	1439.86	9.93
C3-2	16.88	31.54	35.4	1263	974.35	6.72
C4-1	16.81	31.54	35.22	2189	1695.75	11.69
C6-1	16.97	31.49	35.76	2150	1652.46	11.39
C6-2	16.78	31.5	35.38	2321	1803.51	12.43

	Tensile (psi)	Tensile (MPa)
Mean	1384.78	9.55
Median	1402.83	9.67
Std. Dev	270.93	1.87
Min	933.24	6.43
Max	1803.51	12.43

Table 13

Compressive Testing Results from Gypsum

Sample Name	L (mm)	D (mm)	M (g)	X-sectional Area (mm^2)	Density (kg/m^3)	UCS (psi)	UCS (MPa)	E (ksi)	E (Gpa)
E1-1	63.26	29.98	100.28	705.92	2245.51	1307.00	9.01	350.17	2.41
E1-2	63.42	30.26	103.78	719.16	2275.41	1686.00	11.62	229.30	1.58
E2-1	63.23	30.85	107.46	747.48	2273.63	1795.00	12.38	0.00	0.00
E2-2	63.26	30.35	104.29	723.45	2278.71	1944.00	13.40	0.00	0.00
E3-1	63.29	30.19	102.24	715.84	2256.59	1469.00	10.13	177.93	1.23
E3-2	63.25	31.06	110.67	757.69	2309.20	1600.00	11.03	199.79	1.38
F1-1	63.1	30.17	108.16	714.89	2397.71	3095.00	21.34	843.14	5.81
F1-2	63.13	31.14	112.15	761.60	2332.54	4599.00	31.71	1401.15	9.66
F2-1	63.26	30.32	109.68	722.02	2401.21	3556.00	24.52	819.28	5.65
F2-2	63.04	30.51	109.54	731.10	2376.83	4217.00	29.08	1270.55	8.76
F3-1	63.07	31.15	112.57	762.09	2341.94	2480.00	17.10	605.50	4.17
F3-2	62.99	30.9	111.93	749.91	2369.59	4370.00	30.13	1293.24	8.92

	Density (kg/m^3)	UCS (psi)	UCS (MPa)	E (ksi)	E (Gpa)
Mean	2321.57	2676.50	18.45	599.17	4.13
Median	2320.87	2212.00	15.25	477.83	3.29
Std. Dev	55.97	1232.57	8.50	516.76	3.56
Min	2245.51	1307.00	9.01	0.00	0.00
Max	2401.21	4599.00	31.71	1401.15	9.66

Table 14

Tensile Testing Results from Gypsum

Sample Name	Length (mm)	Diameter (mm)	Force (lb)	Strength (psi)	Strength (MPa)
E1-1	16.94	31.21	377	292.87	2.02
E2-1	17.03	29.44	335	274.43	1.89
E3-1	16.70	30.18	373	303.96	2.10
E4-1	17.01	29.86	388	313.75	2.16
E4-2	16.93	30.69	381	301.17	2.08
E5-1	16.75	30.52	498	400.11	2.76
E5-2	16.37	30.51	407	334.70	2.31
E5-3	16.84	30.34	398	319.94	2.21
E5-4	18.26	29.84	382	287.95	1.99
E5-5	16.84	30.54	499	398.51	2.75
F4-1	16.74	30.41	637	513.94	3.54
F4-2	16.72	31.27	633	497.26	3.43
F4-3	16.82	31.34	910	709.03	4.89
F4-4	16.71	31.45	641	500.97	3.45
F4-5	16.87	31.65	1037	797.69	5.50
F5-1	16.91	30.25	529	424.75	2.93
F5-2	15.03	31.08	656	576.78	3.98
F5-3	16.63	30.74	799	641.94	4.43
F5-4	16.48	30.96	709	570.74	3.94
F5-5	16.83	31.47	1388	1076.35	7.42

	Tensile (psi)	Tensile (MPa)
Mean	476.84	3.29
Median	412.43	2.84
Std. Dev	208.01	1.43
Min	274.43	1.89
Max	1076.35	7.42

Table 15

Compressive Testing Results from Limestone Overburden

Sample Name	L (mm)	D (mm)	M (g)	X-sectional Area (mm^2)	Density (kg/m^3)	UCS (psi)	UCS (MPa)	E (ksi)	E (Gpa)
A1-1	64.07	31.50	132.56	779.31	2654.89	20353	140.33	2732.09	18.84
A1-2	64.22	31.49	131.90	778.82	2637.18	18337	126.43	2689.05	18.54
A2-1	63.25	31.49	130.59	778.82	2651.03	21638	149.19	2822.85	19.46
A2-2	63.18	31.50	130.39	779.31	2648.22	18370	126.66	2986.50	20.59
A3-1	63.30	31.46	130.49	777.33	2651.96	19276	132.90	3196.44	22.04
A3-2	63.27	31.48	130.41	778.32	2648.22	20255	139.65	2909.97	20.06
A4-1	62.84	31.47	128.98	777.83	2638.78	19770	136.31	2734.07	18.85
A4-2	63.35	31.46	129.15	777.33	2622.65	18455	127.24	2667.61	18.39
B1-1	63.30	31.33	130.83	770.92	2680.98	31527	217.37	3404.88	23.48
B1-2	63.30	31.33	130.20	770.92	2668.07	28180	194.29	3104.53	21.40
B2-1	63.17	31.28	130.96	768.46	2697.77	26801	184.79	3419.80	23.58
B2-2	63.11	31.36	131.18	772.40	2691.09	28586	197.09	3574.21	24.64
B3-1	63.01	31.37	127.01	772.89	2608.01	23810	164.16	3022.95	20.84
B3-2	63.60	31.50	129.32	779.31	2609.14	22588	155.74	3036.04	20.93
B4-1	63.41	31.45	128.83	776.84	2615.34	19629	135.34	3033.88	20.92
B4-2	62.78	31.51	131.88	779.81	2693.84	26288	181.25	3273.97	22.57

	Density (kg/m^3)	UCS (psi)	UCS (MPa)	E (ksi)	E (Gpa)
Mean	2651.07	22741.44	156.80	3038.05	20.95
Median	2649.62	20995.50	144.76	3028.41	20.88
Std. Dev	29.29	4255.66	29.34	278.52	1.92
Min	2608.01	18337.00	126.43	2667.61	18.39
Max	2697.77	31527.00	217.37	3574.21	24.64

Table 16

Tensile Testing Results from Limestone Overburden

Sample Name	Length (mm)	Diameter (mm)	Force (lb)	Strength (psi)	Strength (MPa)
A5-1	15.98	31.49	2249	1835.635975	12.656263988
A5-2	16.07	31.52	1919	1556.0352451	10.728484899
A5-3	15.72	31.52	1903	1577.4172232	10.875908442
A5-4	16.10	31.52	1975	1598.4592007	11.020987763
A5-5	15.96	31.5	2143	1750.7545789	12.071027388
A6-1	16.03	31.53	2194	1782.8946049	12.292625057
A6-2	15.97	31.51	2191	1788.2803271	12.329758303
A6-3	15.94	31.53	2198	1796.2299809	12.384569234
B5-1	16.07	31.53	2503	2028.9322379	13.98899475
B5-3	16.10	31.43	2087	1693.9427665	11.679323747
B5-4	16.19	31.51	2191	1763.9800385	12.162213718
B5-5	15.93	31.52	2011	1644.9648664	11.341633028
B5-6	15.95	31.53	2020	1649.7314432	11.374497416
B6-1	16.09	31.49	2328	1887.125625	13.011272613
B6-2	16.25	31.48	1921	1542.3602234	10.634198947
B6-3	16.10	31.49	2417	1958.0539531	13.5003062
B6-4	15.84	31.47	2491	2052.4299715	14.151005913
B9-1	15.85	31.54	1856	1524.8725867	10.513625941
B9-2	15.70	31.53	2202	1827.0070875	12.596769906

	Tensile (psi)	Tensile (MPa)
Mean	1750.48	12.07
Median	1763.98	12.16
Std. Dev	159.49	1.10
Min	1524.87	10.51
Max	2052.43	14.15

APPENDIX B

IN-SITU ROCK BLOCK ANALYSIS

Figure 53: Outline of in-situ blocks at Beck Street Quarry

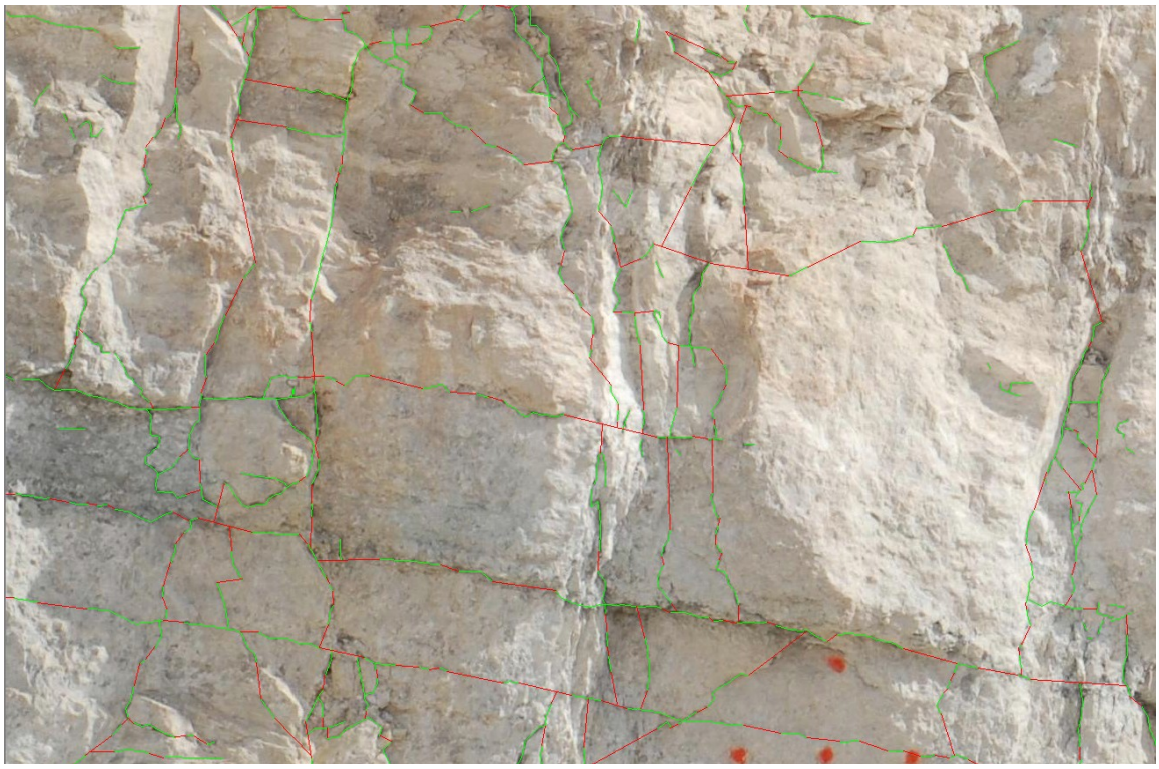

Figure 54: Traces in Limestone Overburden. Joints in green, bridges in red.

Figure 55: Traces in Gypsum. Joints in green, bridges in red.

APPENDIX C

PHOTOGRAPHS OF MUCKPILES

Figure 56: Muckpile at Beck Street Quarry. Printed paper targets for scale.

Figure 57: Muckpile in gypsum blast. Soccer balls for scale.

Figure 58: Muckpile in limestone overburden blast. Soccer balls for scale.

APPENDIX D

ROCK JOINT ORIENTATIONS

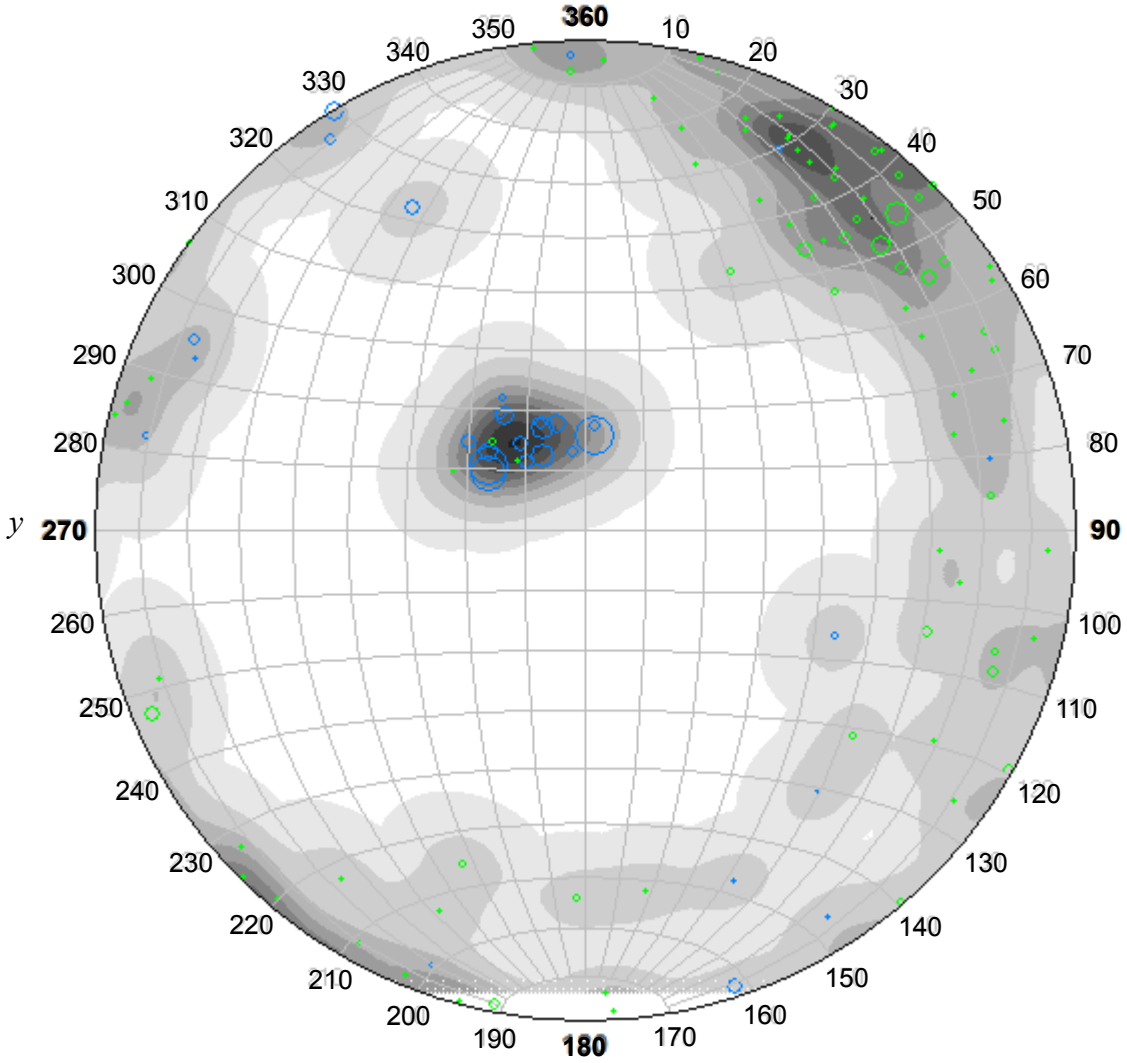

Figure 59: Stereonet pole plot of discontinuities in Beck Street Quarr

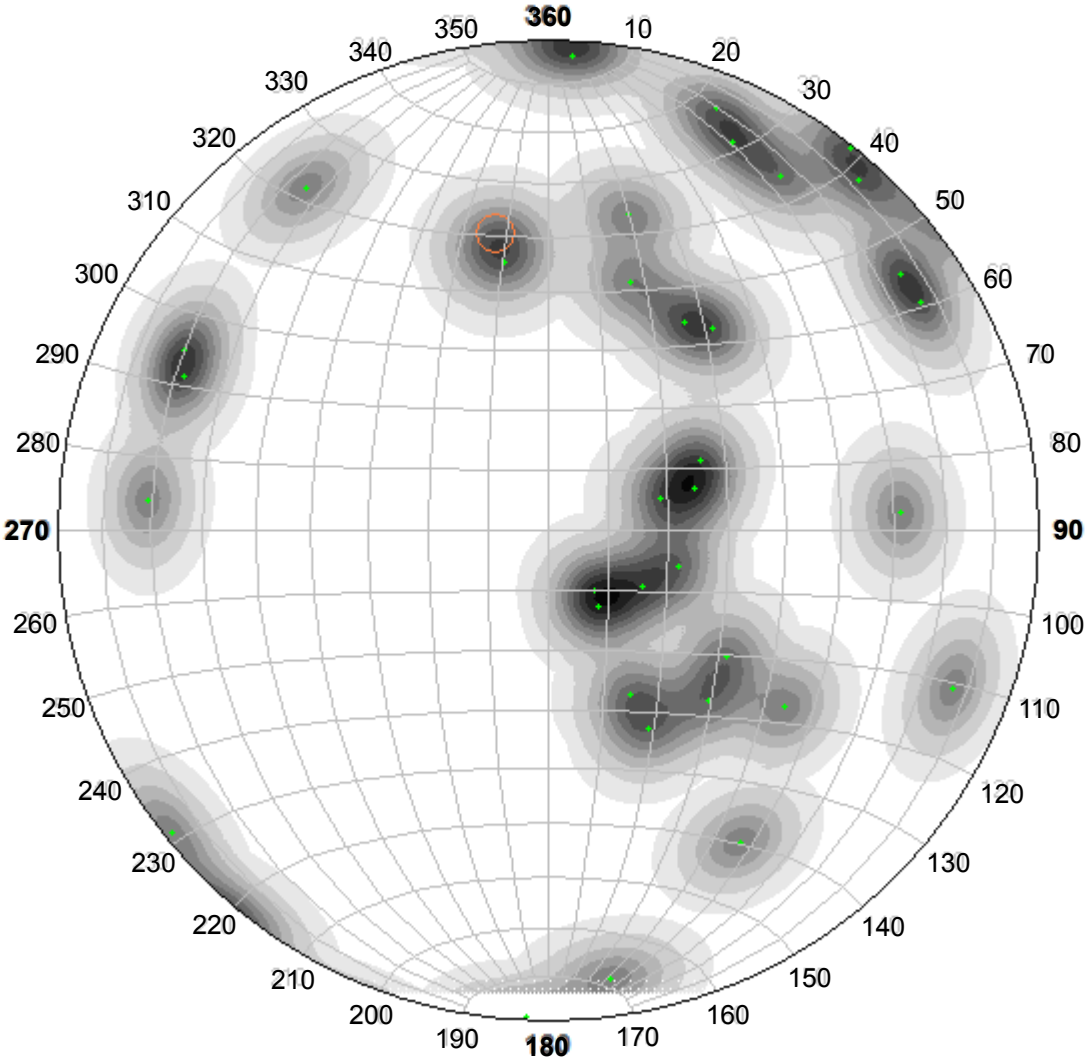

Figure 60: Stereonet pole plot of discontinuities in Gypsum

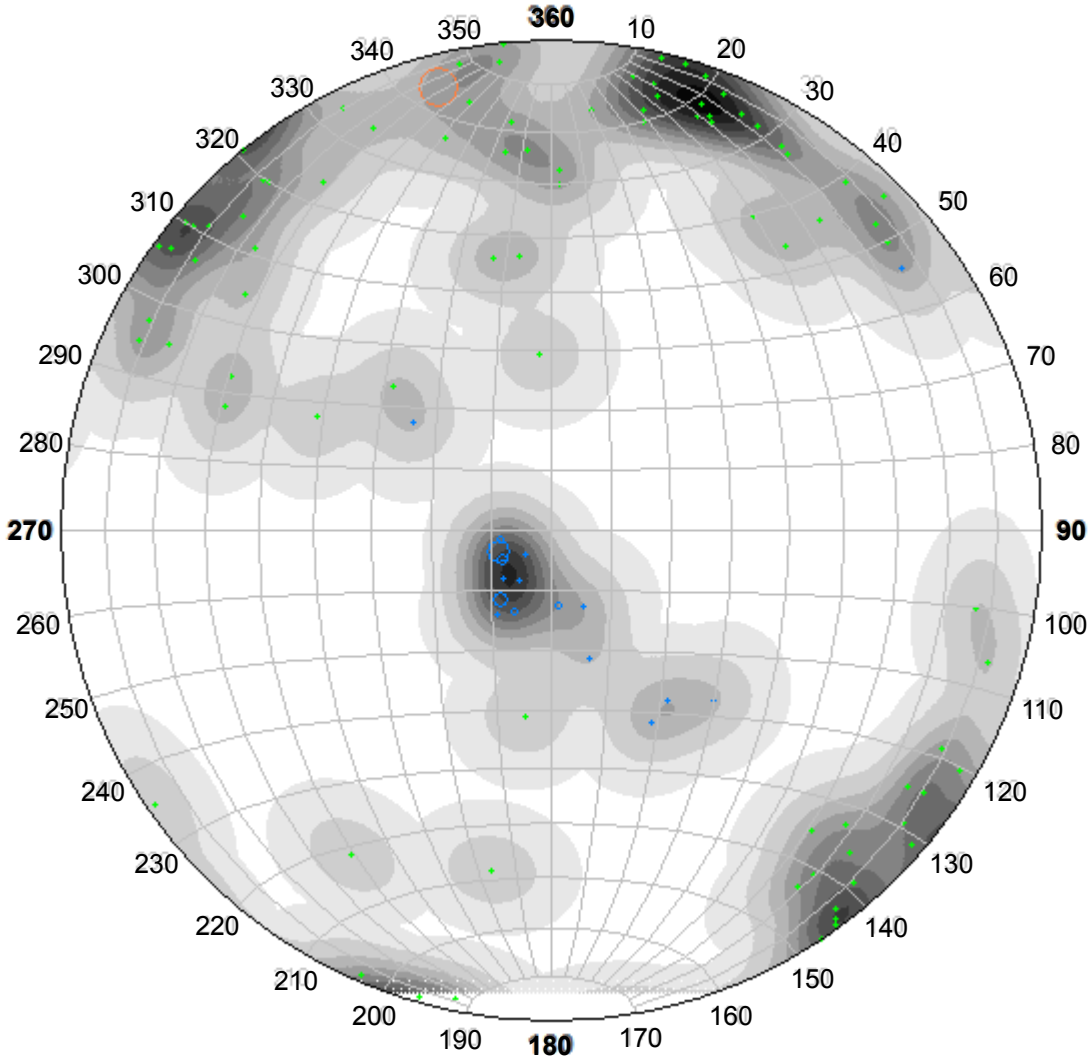

Figure 61: Stereonet pole plot of discontinuities in limestone overburde

REFERENCES

Aydin, A. 2008. ISRM Suggested method for determination of the Schmidt hammer rebound hardness: Revised version. *International Journal of Rock Mechanics and Mining Sciences.* 46(3):627-634

Birch, J.S. Using 3DM Analyst Mine Mapping Suite for Rock Face Characterisation. In *Laser and Photogrammetric Methods for Rock Face Characterization*, Golden, CO, June 2006.

Call, R.D. And Nicholas, D.E. Prediction of step path failure geometry for slope stability analysis. In *Proceedings of the 19th US Symposium on Rock Mechanics*, Reno, NV, May 1978.

Cunningham, C. The Kuz-Ram model for prediction of fragmentation from blasting. In *First International Symposium on Rock Fragmentation by Blasting*, Luleå, Sweden, August 1983.

Donovan, J. and Lebaron, A. A comparison of photogrammetry and laser scanning for the purpose of automated rock mass characterization. In *Proceedings of the 43rd US Rock Mechanics Symposium,* Asheville, NC, June 2009.

Franklin, J.A., Maerz, N.H., and Bennett, C.P. 1988. Rock mass characterization using photoanalysis. *International Journal of Mining and Geological Engineering.* 6(2):97-112

Frayssines, M. and Hantz, D. 2009. Modelling and back-analysing failures in steep limestone cliffs. *International Journal of Rock Mechanics and Mining Sciences*. 46(7):1115- 1123

Gehle, C. and Kutter, H.K. 2003. Breakage and shear behaviour of intermittent rock joints. *International Journal of Rock Mechanics and Mining Sciences.* 40:687-700

Gheibie, S., Aghababaei, H., Hoseinie, S.H., and Pourrahimian, Y. 2009. Modified Kuz-Ram fragmentation model and its use at the Sungun Copper Mine. *International Journal of Rock Mechanics & Mining Sciences*. 46:967-973

Harrison, J.P. Fuzzy objective functions applied to the analysis of discontinuity orientation data. In *ISRM Symposium: Eurock '92*. Chester, UK, September 1992.

Hiramatsu, Y. and Oka, Y. 1966. Determination of the tensile strength of rock by a compression test of an irregular test piece. *International Journal of Rock Mechanics & Mining Sciences*. 3:89-99

Hoek, E. and Brown, E.T. 1980. *Underground Excavations in Rock*. London: The Institute of Mining and Metallurgy.

ISRM. 1985. Suggested method for determining point load strength. *International Journal of Rock Mechanics & Mining Sciences*. 22:51-60

Ivars, D.M., Pierce, M.E., Darcel, C., Reyes-Montes, J., Potyondy, D.O., Young, R.P., and Cundall, P. 2011. The synthetic rock mass approach for jointed rock mass modelling. *International Journal of Rock Mechanics & Mining Sciences*. 48:219-244

Jimenez-Rodriguez, R. and Sitar, N. A spectral method for clustering of rock discontinuity sets. *International Journal of Rock Mechanics & Mining Sciences*. 43(7):1052-1061

Katz, O., Reches, Z., and Roegiers, J.C. 2000. Evaluation of mechanical rock properties using a Schmidt Hammer. *International Journal of Rock Mechanics and Mining Sciences.* 37:723-728

Kuznetsov, V.M. 1973. The mean diameter of the fragments formed by blasting rock. *Soviet Mining Science.* 9(2):144-148

Levy, M.L. And Visca, P.J. Statistical characterization of rock structure using LiDAR. In *Proceedings of the 43rd US Rock Mechanics Symposium and 4th U.S.-Canada Rock Mechanics Symposium,* Asheville, NC, June 2008.

Pariseau, W.G. 2007. *Design Analysis in Rock Mechanics*. London: Taylor & Francis.

Pariseau, W.G., Puri, S., and Schmelter, S.C. 2008. A new model for effects of impersistent joint sets on rock slope stability. *International Journal of Rock Mechanics and Mining Science.* 45(2):122-131

Persson, P., Holmberg, R., Lee, J. 1994. *Rock Blasting and Explosives Engineering*. Boca Raton, FL: CRC Press

Rodriguez, R.J. And Sitar, N. A. 2006. A spectral method for clustering of rock discontinuity sets. *International Journal of Rock Mechanics and Mining Science.* 43:1056-1061

Rosin, P. and Rammler, E. 1933. The laws governing the fineness of powdered coal. *Journal of the Institute of Fuels*. 7:29-36

Russell, A.R. And Wood, D.M. 2009. Point load tests and strength measurements for brittle spheres. *International Journal of Rock Mechanics and Mining Science.* 46:272-280

Schmidt, E. 1951. A non-destructive concrete tester. *Concrete*. 59(8):34-35

Soole, P. and Poropat, G. Highwall mapping using terrestrial photogrammetry. In *Bowen Basin Symposium 2000 Proceedings*, Rockhampton, October 2000.

Sturzenegger, M. and Stead, D. 2009. Quantifying discontinuity and persistence on high mountain rock slopes and large landslides using terrestrial remote sensing techniques. *Nat. Hazards Earth Syst. Sci.* (9):267-287

Sturzenegger, M. and Stead, D. 2009. Close-range terrestrial digital photogrammetry and terrestrial laser scanning for discontinuity characterization on rock cuts. *Engineering Geology.* 106:163-182

Terzaghi, R.D. 1965. Sources of error in joint surveys. *Geotechnique.* 15(3):287-304.

U.S. Department of Energy. 2006. *Mine-to-Mill Optimization*. http://www.netl.doe.gov/keyissues/mining/minetomill.pdf. Accessed May 2011.

ADAM Technology. 2010. How accurate is photogrammetry?-Part 2. www.adamtech.com.au/Blog/?p=167. Accessed November 2010.